JACS
JOURNAL OF THE AMERICAN CHEMICAL SOCIETY
Article
pubs.acs.org/JACS

Cyanide Single-Molecule Magnets Exhibiting Solvent Dependent Reversible "On" and "Off" Exchange Bias Behavior

Dawid Pinkowicz,[*,†] Heather I. Southerland,[‡] Carolina Avendaño,[‡] Andrey Prosvirin,[‡] Codi Sanders,[‡] Wolfgang Wernsdorfer,[§] Kasper S. Pedersen,[∥,#,∇] Jan Dreiser,[⊥] Rodolphe Clérac,[#,∇] Joscha Nehrkorn,[○,◆] Giovanna G. Simeoni,[¶] Alexander Schnegg,[○,◆] Karsten Holldack,[+] and Kim R. Dunbar[*,‡]

[†]Faculty of Chemistry, Jagiellonian University, Ingardena 3, 30-060 Kraków, Poland

[‡]Department of Chemistry, Texas A&M University, College Station, Texas 77842-3012, United States

[§]Institute Néel, CNRS, BP 166, 25 Avenue de Martyrs, Grenoble, 38042 Cedex 9, France

[∥]Department of Chemistry, University of Copenhagen, Universitetsparken 5, DK-2100 Copenhagen, Denmark

[⊥]Institute of Condensed Matter Physics, Ecole Polytechnique Fédérale de Lausanne, CH-1015 Lausanne, Switzerland and Swiss Light Source, Paul Scherrer Insitut, CH-5232 Villigen PSI, Switzerland

[#]CNRS, CRPP, UPR 8641, F-33600 Pessac, France

[∇]Univ. Bordeaux, CRPP, UPR 8641, F-33600 Pessac, France

[○]Institut Nanospektroskopie, Helmholtz-Zentrum Berlin für Materialien und Energie, Kekulestr. 5, D-12489 Berlin, Germany

[◆]Berlin Joint EPR Laboratory, Helmholtz-Zentrum Berlin für Materialien und Energie, Kekulestr. 5, D-12489 Berlin, Germany

[¶]Heinz Meier-Leibnitz Zentrum (MLZ) and Physics Department, Technical University of Munich, Lichtenbergstr. 1, 85748 Garching, Germany

[+]Institut für Methoden und Instrumentierung der Forschung mit Synchrotronstrahlung, Albert-Einstein-Str. 15, D-12489 Berlin, Germany

Supporting Information

ABSTRACT: The syntheses, structures, and magnetic properties of four new complex salts, (PPN){[Mn^{III}(salphen)(MeOH)]$_2$[M^{III}(CN)$_6$]}·7MeOH (Mn_2M·7MeOH) (M = Fe, Ru, Os and Co; PPN^+ = bis(triphenylphosphoranylidene)ammonium cation; H_2salphen = *N*,*N*′-bis(salicylidene)-1,2-diaminobenzene), and a mixed metal Co/Os analogue (PPN){[Mn^{III}(salphen)(MeOH)]$_2$[$Co^{III}_{0.92}Os^{III}_{0.08}(CN)_6$]}·7MeOH were undertaken. It was found that all compounds exhibit switchable single-molecule magnet (SMM) and exchange-bias behavior depending on the interstitial methanol content. The pristine (PPN){[Mn(salphen)(MeOH)]$_2$[Os(CN)$_6$]}·7MeOH (Mn_2Os·7MeOH) behaves as an SMM with an effective barrier for the magnetization reversal, (U_{eff}/k_B), of 17.1 K. Upon desolvation, Mn_2Os exhibits an increase of U_{eff}/k_B to 42.0 K and an opening of the hysteresis loop observable at 1.8 K. Mn_2Os·7MeOH shows also exchange-bias behavior with magnetic hysteresis loops exhibiting a shift in the quantum tunneling to 0.25 T from zero-field. The Fe^{III} and Ru^{III} analogues were prepared as reference compounds for assessing the effect of the 5d versus 4d and 3d metal ions on the SMM properties. These compounds are also SMMs and exhibit similar effects but with lower energy barriers. These findings underscore the importance of introducing heavy transition elements into SMMs to improve their slow relaxation of the magnetization properties. The (PPN){[Mn^{III}(salphen)(MeOH)]$_2$[Co^{III}(CN)$_6$]}·7MeOH (Mn_2Co·7MeOH) analogue with a diamagnetic Co^{III} central atom and the mixed Co/Os (PPN){[Mn^{III}(salphen)(MeOH)]$_2$[$Co^{III}_{0.92}Os^{III}_{0.08}(CN)_6$]}·7MeOH ($Mn_2Co/Os$·7MeOH) "magnetically diluted" system with a 9:1 Co/Os metal ratio were prepared in order to further probe the nature of the energy barrier increase upon desolvation of Mn_2Os. In addition, inelastic neutron scattering and frequency-domain Fourier-transform THz electron paramagnetic resonance spectra obtained on Mn_2Os·7MeOH and Mn_2Os in combination with the magnetic data revealed the presence of anisotropic exchange interactions between Mn^{III} and Os^{III} ions.

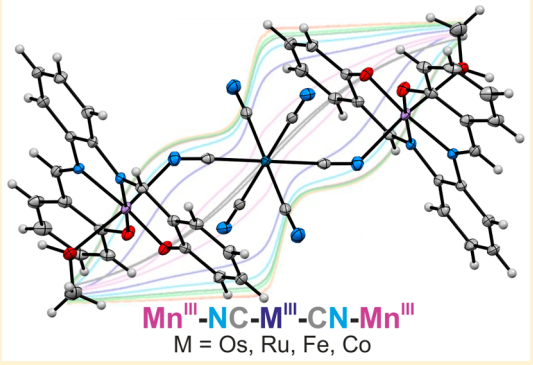

Received: September 4, 2015
Published: November 6, 2015

DOI: 10.1021/jacs.5b09378
J. Am. Chem. Soc. 2015, 137, 14406−14422

INTRODUCTION

Mixed-metal cyanide compounds constitute an excellent platform for studying magnetic bistability in molecules commonly referred to as single-molecule magnets (SMMs), a term that was coined in the mid-1990s to describe molecules that exhibit slow relaxation of their magnetization.[1−17] Since the discovery of slow paramagnetic dynamics in $[Mn_{12}O_{12}(O_2CCH_3)_{16}(H_2O)_4]$ (Mn12−Ac),[18−21] considerable effort has been directed toward the goal of increasing the intrinsic barrier height for magnetization reversal, U, which is equal to $S^2|D|$ for integer S values and $(S^2 - 1/4)|D|$ for half-integer S with D being the axial component of the magnetic anisotropy (considering the following Hamiltonian of anisotropy: $H = DS_z^2$). Much of the research in this area has focused on increasing the barrier by preparing molecules with large spin ground states (S) but this approach has not led to an appreciable increase in the barrier height of SMMs.[22−26]

In response to the inherent challenges of enhancing SMM properties, researchers have turned to the task of increasing anisotropy with considerable progress having been realized as evidenced by the discovery of numerous small molecule and even mononuclear SMMs.[27−43] One of the successful strategies is to incorporate 4d and 5d transition metal ions into mixed metal complexes.[44−47] These ions are characterized by large spin−orbit coupling (SOC) parameters which contribute to the orbital angular momenta and also, depending on the symmetry of the complex, lead to anisotropic exchange interactions. Of importance in this context is the fact that theoretical work has predicted that single ion anisotropy originating from spin−orbit coupling will lead to higher blocking temperatures, T_B, for SMMs.[25,48−55] A convenient method for testing this hypothesis is to target heavy element cyanide-bridged complexes combined with 3d transition metals. Illustrations of the effective implementation of this approach are the reports of trinuclear $\{[Mn^{II}(L_{N5Me})(H_2O)]_2[Mo^{III}(CN)_7]\cdot 6H_2O\}$,[6] pentanuclear $\{[Mn^{II}(py5Me_2)]_4[Re^{IV}(CN)_7][PF_6]_5$,[56] heptanuclear $K\{[(Me_3tacn)Mo^{III}(CN)_3]_6Mn^{II}\}[ClO_4]_3$,[57] and octanuclear $\{[(triphos)Re^{II}(CN)_3]_4[Mn^{II}Cl]_4\}$[58,59] complexes, all of which are SMMs.

Another important development in the field of SMMs is the recent exploration of the effect of exchange-bias[60−69] which occurs when weak magnetic interactions occur between neighboring SMMs causing a shift in the quantum tunneling of the magnetization (QTM) from zero-field. These magnetic exchange interactions are capable of breaking the degeneracy of the energy levels such that there is a quantum interference associated with the spin of the molecule and the QTM is shifted.[70] Understanding and fine-tuning these weak intermolecular interactions for the control of the QTM in SMMs are important steps in the eventual use of SMMs in storage and switching devices.[62,66] Recent studies have also focused on various switchable SMMs for which the dynamics of slow relaxation is triggered/modulated by light,[71−73] guest molecules,[74] or redox changes.[75,76]

One simple class of SMM molecules with bridging cyanide ligands is the family of linear trinuclear complexes with Mn^{III} Schiff base terminal units bridged by hexacyanometallate building blocks.[77−82] In the current study, we are using $\{Mn^{III}(salphen)(MeOH)\}^+$ as a capping group for the synthesis of new trinuclear SMMs of $[Fe^{III}(CN)_6]^{3-}$, $[Ru^{III}(CN)_6]^{3-}$, $[Os^{III}(CN)_6]^{3-}$, and $[Co^{III}(CN)_6]^{3-}$ of general formula: $(PPN)\{[Mn^{III}(salphen)(MeOH)]_2[M^{III}(CN)_6]\}\cdot 7MeOH$ ($Mn_2M\cdot 7MeOH$) (M = Fe, Ru, Os, and Co; PPN^+ = bis(triphenylphosphoranylidene)ammonium cation; H_2-salphen = *N*,*N*′-bis(salicylidene)-1,2-diaminobenzene). The use of the salphen^{2-} ligand promotes supramolecular interactions which are not present in the related SMMs with other salen-type ligands[77−82] and which appear to be crucial for controlling resonant quantum tunneling via weak intermolecular antiferromagnetic interactions.

EXPERIMENTAL DETAILS

Materials. All chemicals and solvents were of reagent grade purity or higher. The compounds OsO_4, $RuCl_3$, $K_3[Fe(CN)_6]$, $K_3[Co(CN)_6]$, $Mn(ClO_4)_2\cdot xH_2O$, $Ce(SO_4)_2$, and PPNCl (PPN = bis(triphenylphosphoranylidene)ammonium) were purchased from Sigma-Aldrich and used as received. The tetradentate Schiff-base ligand H_2-salphen was prepared by mixing the 2-salicylaldehyde and *o*-phenylenediamine in a 2:1 mol ratio in ethanol, according to the literature procedures.[83,84] The $K_4[Os(CN)_6]\cdot 3H_2O$[85] and $K_4[Ru(CN)_6]$[86,87] salts were prepared as previously reported.

Starting Materials. *$(PPN)_3[Os(CN)_6]\cdot H_2O$.* A sample of $K_4[Os(CN)_6]\cdot 3H_2O$ (1 g, 2 mmol) was dissolved in 50 mL of H_2O and stirred for 20 min to give a clear, colorless solution. This solution was then treated with $Ce^{IV}(SO_4)_2$ (0.662 g, 2 mmol) which led to an instantaneous change to yellow followed by green and finally back to greenish-yellow. The yellow solution was quickly filtered, and the filtrate was heated to ∼50 °C and then slowly added to a hot (∼60 °C) solution of PPNCl (3.4 g, 6 mmol). This led to the formation of a yellowish-green fluffy solid collected by filtration, treated with three portions of hot water (100 mL each) to dissolve impurities, and finally washed with 100 mL of diethyl ether. The crude product was recrystallized from MeOH/THF/Et_2O in the form of small light-green crystals and dried. Average yield: 55%. Elemental Analysis (EA): Calcd for $C_{114}H_{90}N_9OOsP_6$ (%): C, 69.15; H, 4.68; N, 6.37. Found: C, 68.70; H, 4.84; N, 6.38. Single crystal X-ray structural analysis was performed, and the compound was found to crystallize in an orthorhombic *Pbcn* space group. Crystallographic details with a structural diagram of the asymmetric unit can be found in the Supporting Information (Table S1 and Figure S1). The salt $(PPN)_3[Os(CN)_6]\cdot H_2O$ is isomorphous with the previously published $(PPN)_3[Fe(CN)_6]\cdot H_2O$ analogue.[88]

$(PPN)_3[Ru(CN)_6]\cdot H_2O$. This salt was prepared by the same procedure as described for $(PPN)_3[Os(CN)_6]\cdot H_2O$. Average yield: ∼59%. Elemental Analysis (EA): Calcd for $C_{114}H_{90}N_9ORuP_6$ (%): C, 72.41; H, 4.90; N, 6.67. Found: C, 72.24; H, 5.08; N, 6.60. Single crystal X-ray structural analysis has been performed. The compound crystallizes in an orthorhombic *Pbcn* space group. Crystallographic details with a structural diagram of the asymmetric unit can be found in the Supporting Information (Table S1 and Figure S1). Only half of the H_2O molecule per $[Ru^{III}(CN)_6]$ moiety was located in the crystal structure due to disorder and partial dehydration. $(PPN)_3[Ru(CN)_6]\cdot H_2O$ is isomorphous with the previously published $(PPN)_3[Fe(CN)_6]\cdot H_2O$ compound.[88]

$(PPN)_3[Fe(CN)_6]\cdot H_2O$. This salt was prepared by a previously reported procedure.[88] A warm (∼45 °C) aqueous solution (20 mL) of $K_3[Fe(CN)_6]$ (0.3 g; 0.91 mmol) was added dropwise to a warm stirring solution of PPNCl (1.57 g, 2.74 mmol) in 60 mL of water. Instantaneous formation of a microcrystalline yellow precipitate occurs. After stirring the mixture for 10 min, the solid was collected by filtration in air, washed with warm water, and dried. The product was recrystallized from MeOH/THF/Et_2O and vacuum-dried. Yield: 1.48 g (88%).

$(PPN)_3[Co(CN)_6]\cdot H_2O$. This salt was prepared in the same manner as $(PPN)_3[Fe(CN)_6]\cdot H_2O$ using $K_3[Co(CN)_6]$.

$[Mn^{III}(salphen)(H_2O)][ClO_4]\cdot 2H_2O$. This starting material was synthesized using a modified procedure from a previous report.[83,84] To a yellow suspension of salphenH_2 (2.53 g, 8.0 mmol) in an ethanol/methanol mixture (1:1, 40 mL) was added a solution of

DOI: 10.1021/jacs.5b09378
J. Am. Chem. Soc. 2015, 137, 14406−14422

$Mn(ClO_4)_2{\cdot}xH_2O$ (2.80 g, 8.0 mmol; anhydrous calc) in 10 mL of ethanol. The initial yellow mixture was stirred for 10 min during which time a color change to dark brown occurred. An equimolar amount of potassium hydroxide (0.45 g, 8.0 mmol) dissolved in 4 mL of ethanol was then added dropwise to avoid the precipitation of manganese oxides and the reaction mixture became darker.

The resulting mixture was heated gently and stirred for 2 days while bubbling air through it. During this time, the mixture was concentrated to about 1/3 of the initial volume and became dark brown with only a small amount of solid on the bottom. The mixture was filtered through a glass frit to remove a small amount of white solid which was discarded. The filtrate was treated with a 3-fold excess of diethyl ether (slow addition) with stirring which led to the isolation of a brown-black crystalline solid. The product was collected by filtration, washed with diethyl ether (3 × 10 mL) and dried in vacuo. Typical yield: 2.5 g (~60%).

Preparation of Compounds. *(PPN){[Mn(salphen)(MeOH)]$_2$[Os(CN)$_6$]}·7MeOH (Mn$_2$Os·7MeOH).* A solution of $(PPN)_3[Os^{III}(CN)_6]\cdot H_2O$ (196 mg, 0.1 mmol) in methanol (28 mL) was added to a methanolic solution (31 mL) of $[Mn^{III}(salphen)(H_2O)][ClO_4]\cdot 2H_2O$ (90 mg, 0.16 mmol). The resulting dark-red solution was left undisturbed for crystallization (typically 12−48 h). The product in the form of dark red platelet crystals was collected by filtration, washed with a minimal amount of methanol and dried very briefly in air as the compound readily loses crystallization solvent (MeOH). Yield: 70 mg (37%; typically 30−50% depending on the crystallization time and the scale of the synthesis). Elemental analysis (EA) data for a freshly prepared sample: Calcd for $C_{91}H_{94}Mn_2N_{11}O_{13}OsP_2$ (%): C, 57.17; H, 4.96; N, 8.06. Found: C, 56.90; H, 4.78; N, 8.48. EA for a vacuum-dried sample (12 h, 10 mbar): Calcd for $C_{84}H_{66}Mn_2N_{11}O_6OsP_2$ (%): C, 59.78; H, 3.94; N, 9.13. Found: C, 60.00; H, 3.44; N, 9.34. The purity/identity of the sample was confirmed additionally by powder X-ray diffraction (PXRD) on a freshly prepared sample (Figure 1). The experimental pattern is in good agreement with the simulated one obtained from room temperature single-crystal data and the experimental patterns of other analogues.

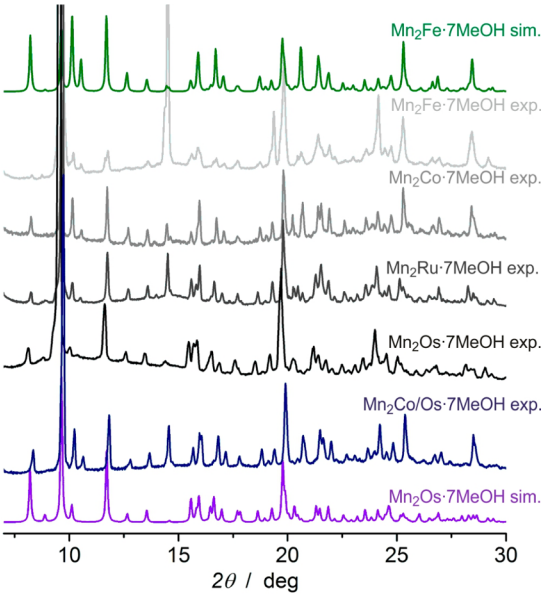

Figure 1. Powder X-ray diffraction patterns of the reported compounds: simulated from single crystal data for Mn$_2$Fe·7MeOH collected at room temperature (first), experimental for Mn$_2$Fe·7MeOH (second), experimental for Mn$_2$Co·7MeOH (third), experimental for Mn$_2$Ru·7MeOH (fourth), experimental for Mn$_2$Os·7MeOH (fifth), experimental for Mn$_2$Co/Os·7MeOH (sixth), and simulated from single crystal data for Mn$_2$Os·7MeOH collected at room temperature (seventh). Slight differences in the intensity of some peaks are due to orientation effects (texture).

(PPN){[Mn(salphen)(MeOH)]$_2$[Fe(CN)$_6$]}·7MeOH (Mn$_2$Fe·7MeOH). This compound was obtained by the same procedure as described for (Mn$_2$Os·7MeOH). $(PPN)_3[Fe^{III}(CN)_6]\cdot H_2O$ (182 mg, 0.1 mmol) in methanol (30 mL) was added to a methanolic solution (30 mL) of $[Mn^{III}(salphen)(H_2O)][ClO_4]\cdot 2H_2O$ (90 mg, 0.16 mmol). The resulting clear dark red solution was left undisturbed for crystallization (typically 12−48 h). The product in the form of dark red platelet crystals was collected by filtration and washed with a minimal amount of methanol and dried very briefly in air. The compound loses crystallization solvent (MeOH) readily. Yield: 61 mg (34%; typically 30−50% depending on the crystallization time and the scale of the synthesis). Elemental analysis (EA) data for a freshly prepared sample: Calcd for $C_{91}H_{94}FeMn_2N_{11}O_{13}P_2$ (%): C, 61.49; H, 5.33; N, 8.67. Found: C, 61.11; H, 5.26; N, 8.98. EA for a vacuum-dried sample (12 h, 10 mbar): Calcd for $C_{84}H_{66}FeMn_2N_{11}O_6P_2$ (%): C, 64.96; H, 4.28; N, 9.92. Found: C, 65.41; H, 4.04; N, 10.39. The purity was confirmed additionally by PXRD on a freshly prepared sample (Figure 1).

(PPN){[Mn(salphen)(MeOH)]$_2$[Ru(CN)$_6$]}·7MeOH (Mn$_2$Ru·7MeOH). This compound was obtained by the same procedure as described for (Mn$_2$Os·7MeOH). $(PPN)_3[Ru^{III}(CN)_6]\cdot H_2O$ (99 mg, 0.05 mmol) in methanol (12.5 mL) was added to the methanolic solution (12.5 mL) of $[Mn^{III}(salphen)(H_2O)][ClO_4]\cdot 2H_2O$ (45 mg, 0.086 mmol). The resulting clear dark red solution was left undisturbed for crystallization (typically 12−20 h; longer times lead to decomposition). The resulting dark red needle crystals were collected by filtration and washed with a minimal amount of methanol and dried for a brief period of time in air. The compound rapidly loses interstitial MeOH molecules. Yield: 13 mg (14%; typically 10−20% depending on the crystallization time and the scale of the synthesis). Elemental analysis (EA) data for a freshly prepared sample: Calcd for $C_{91}H_{94}Mn_2N_{11}O_{13}P_2Ru$ (%): C, 59.97; H, 5.20; N, 8.45. Found: C, 61.10; H, 4.77; N, 8.85. EA for a vacuum-dried sample (12 h, 10 mbar): Calcd for $C_{84}H_{66}Mn_2N_{11}O_6P_2Ru$ (%): C, 63.32; H, 4.25; N, 9.56. Found: C, 63.51; H, 3.90; N, 10.05. The purity/identity of the sample was also confirmed by PXRD on freshly prepared sample (Figure 1).

(PPN){[Mn(salphen)(MeOH)]$_2$[Co(CN)$_6$]}·7MeOH (Mn$_2$Co·7MeOH). This compound was obtained by the same procedure as described for Mn$_2$Os·7MeOH with a slight modification due to the presence of *{[Mn(salphen)(MeOH)$_2$]$_3$[Co(CN)$_6$]}·6MeOH* (Mn$_3$Co·6MeOH; large dark red needles; see Table S1 and Figure S1 in the Supporting Information) as a persistent impurity. $(PPN)_3[Co^{III}(CN)_6]\cdot H_2O$ (286 mg, 0.16 mmol) in methanol (12.5 mL) was added to a methanolic solution (51 mL) of $[Mn^{III}(salphen)(H_2O)][ClO_4]\cdot 2H_2O$ (120 mg, 0.23 mmol). The resulting dark red solution was left undisturbed for crystallization (typically 12−48 h). The product crystallizes as small dark red platelet crystals with the impurity crystallizing as large needles. A small crop of plate-like crystals of Mn$_2$Co·7MeOH was separated mechanically and washed with a small amount of fresh MeOH. The synthesis was repeated and the Mn$_2$Co·7MeOH crystals were used for seeding. In this way pure bulk Mn$_2$Co·7MeOH was obtained. The compound readily loses crystallization solvent (MeOH). Yield: 33 mg (16%; typically 10−20% depending on the crystallization time and the scale of the synthesis). Elemental analysis (EA) data for a freshly prepared sample: Calcd for $C_{91}CoH_{94}Mn_2N_{11}O_{13}P_2$ (%): C, 61.38; H, 5.32; N, 8.65. Found: C, 61.09; H, 4.78; N, 8.98. EA for a vacuum-dried sample (12 h, 10 mbar): Calcd for $C_{84}CoH_{66}Mn_2N_{11}O_6P_2$ (%): C, 64.83; H, 4.27; N, 9.90. Found: C, 64.56; H, 3.77; N, 10.43. It is worth noting that impurities analogous to the {[Mn(salphen)(MeOH)]$_3$[Co(CN)$_6$]}·xMeOH synthesis were not observed for other Mn$_2$M·7MeOH compounds. The purity/identity of the sample was confirmed by PXRD on a freshly prepared sample (Figure 1).

(PPN){[Mn^{III}(salphen)]$_2$[Co$^{III}_{0.92}$Os$^{III}_{0.08}$(CN)$_6$]}·7MeOH (Mn$_2$Co/Os·7MeOH). The mixed Co/Os compound Mn$_2$Co/Os·7MeOH was obtained from the reaction mixture containing an approximate 9:1 molar ratio of $[Co^{III}(CN)_6]^{3-}$ and $[Os^{III}(CN)_6]^{3-}$ by the same procedure as described for (Mn$_2$Co·7MeOH) with seeding. Elemental Analysis (EA) for freshly prepared sample: Calcd for $C_{91}Co_{0.92}H_{94}Mn_2N_{11}O_{13}Os_{0.08}P_2$ (%): C, 61.02; H, 5.29; N, 8.60. Found: C,

DOI: 10.1021/jacs.5b09378
J. Am. Chem. Soc. 2015, 137, 14406−14422

60.63; H, 4.94; N, 8.93. EA for a vacuum-dried sample (12 h, 10 mbar): Calcd for C_{84} $Co_{0.92}H_{66}Mn_2N_{11}O_6Os_{0.08}P_2$ (%): C, 64.39; H, 4.25; N, 9.83. Found: C, 63.64; H, 3.73; N, 9.87. Both EAs support the approximately 9:1 Co:Os molar ratio in the samples. The purity/identity of the pristine state was confirmed additionally by PXRD on a freshly prepared sample (Figure 1).

Single Crystal X-ray Crystallography. For a typical low-temperature experiment for all compounds, a crystal was selected for study and mounted on a cryoloop using low-temperature immersion oil and placed in a N_2 cold stream. Single-crystal X-ray data were collected on a Bruker APEXII diffractometer (MoKα radiation) equipped with a CCD detector at 110 K. The data sets were recorded as three or four ω-scans and integrated with the Bruker SAINT[17] software package. The absorption correction (Bruker SADABS[17]) was based on fitting a function to the empirical transmission surface as sampled by multiple equivalent measurements. Solution and refinement of the crystal structures were carried out using SIR-92[18] and SHELX[89] within the WinGX package.[90] Structure solution by direct methods resolved positions of all metal atoms as well as most of the P, C and N atoms. The remaining non-hydrogen atoms were located by alternating cycles of least-squares refinements and difference Fourier maps. Hydrogen atoms were placed at calculated positions. The final refinements were performed with anisotropic thermal parameters for all non-hydrogen atoms. A summary of pertinent information relating to unit cell parameters, data collection, and refinement is provided in Tables 1 and S1. Selected metal−ligand bond distances and angles are provided in Table S2.

For room temperature single crystal XRD experiments the crystals of Mn_2Fe·7MeOH and Mn_2Os·7MeOH were mounted in a sealed borosilicate capillary with a drop of methanol to prevent decomposition during data collection. The measurements and analyses of the data sets were performed as described above (Supporting Information, Table S1). For crystals of Mn_2Co/Os·7MeOH, the Co and Os atoms could only be refined anisotropically with 0.92 and 0.08, respective occupancy, which confirms the intended 9−10% diamagnetic dilution.

Powder X-ray Crystallography. Powder X-ray data were recorded at room temperature on a Bruker D8-Focus Bragg−Brentano diffractometer (Cu Kα radiation) with 0.02° steps in the 2θ range of 5−50°. The total data collection time was 60 min. Typically, 8−12 mg of the sample was ground under a coating of methanol and the suspension was transferred onto the Si reflection-less flat sample holder. The sample was protected from solvent loss with parafilm. The preparation of the sample and its morphology (plates) cause moderate orientation issues that influence the intensity of some peaks in the experimental patterns.

Magnetic Measurements. Magnetic data were collected on samples of crushed crystals with the use of a Quantum Design MPMS-XL SQUID magnetometer; samples were measured in custom delrin sample holders with a screw cap developed in our laboratories. The pristine samples were loaded into the holders with a quantity of MeOH (typically ∼30 mg) covering the sample and were sealed tightly to prevent solvent loss during the measurements. In the case of the desolvated forms, the holders containing the solvated crystals and methanol were opened carefully and were subjected to vacuum for 5−7 h (ca. 0.1 mbar), closed tightly, and remeasured. For magnetic measurements of the resolvated forms, the holders containing the desolvated samples were opened, a quantity of MeOH (typically ∼20 mg) was added and the holders were closed tightly. DC magnetic susceptibility measurements were performed in the range of 1.8−300 K under an applied field of 1000 Oe. AC magnetic susceptibility measurements were performed with a 5 Oe AC oscillating field in an operating frequency range of 1−1500 Hz. Magnetization data were collected in the −70 to 70 kOe field range at 1.8 K. The data were corrected for the diamagnetic contribution of the sample holders (point-by-point subtraction of the background), the quantity of methanol covering the samples and the sample diamamagnetism from the Pascal constants. MicroSQUID measurements were collected on oriented single crystals in the easy magnetization direction at the temperatures indicated and in fields up to 1.4 T with sweep rates up to 0.28 T/s. Temperature dependence of the magnetic susceptibility were fit using the isotropic Heisenberg−Dirac−Van Vleck Hamiltonian assuming an external magnetic field H:

$$H = -2J_{\mathrm{Mn-M}}(S_{\mathrm{Mn1}}\tau_{\mathrm{M}} + S_{\mathrm{Mn2}}\tau_{\mathrm{M}}) + D_{\mathrm{Mn}}(S_{\mathrm{Mn1},z}{}^2 + S_{\mathrm{Mn2},z}{}^2) + \mu_{\mathrm{B}}\mu_0 H_Z(g_{\mathrm{Mn}}(S_{\mathrm{Mn1},z} + S_{\mathrm{Mn2},z}) + g_{\mathrm{effM}}\tau_{\mathrm{M},z}) \quad (1)$$

where $J_{\mathrm{Mn-M}}$ is the isotropic exchange constant (allowed to vary); M corresponds to the central metal ion Co, Fe, Ru, or Os; S_{Mn1} and S_{Mn2} are the spin operators for the two Mn metal centers; τ_{M} is the pseudospin-1/2 operator that describes the ground state of the M metal center; g_{Mn} is the g factor of Mn centers (fixed), D_{Mn} is the zero-field splitting parameter of Mn (fixed), and g_{effM} is the effective g factor (fixed) for Fe, Ru, or Os, respectively.[82] The fitting of the magnetic susceptibility and the simulation of the magnetization were carried out using PHI software.[91] The intermolecular interactions were included within the mean-field (MF) approximation[92,93] (incorporated in PHI 2.0) by applying the following analytical formula assuming g = 2.0 for the whole Mn_2M complex:

$$\chi_{MF} = \frac{\chi_{\mathrm{complex}}}{1 - \frac{2zJ'}{Ng^2\mu_{\mathrm{B}}{}^2}\chi_{\mathrm{complex}}} \quad (2)$$

PHI 2.0 manual indicates that zJ' is calculated within the $H = -JS_1S_2$ formalism using a slightly different formula that does not include the g factor:

$$\chi_{\mathrm{MF}} = \frac{\chi_{\mathrm{complex}}}{1 - \frac{zJ'}{N\mu_{\mathrm{B}}{}^2}\chi_{\mathrm{complex}}} \quad (3)$$

Therefore, the zJ' values calculated from the PHI program were multiplied by a factor of 2 (assuming g = 2.0) in order to make them consistent with eq 2 and with the $H = -2JS_1S_2$ formalism used in this paper.

Since all reported compounds are based on highly anisotropic metal ions, magnetic susceptibility and magnetization were calculated by using the Zaremba−Conroy−Wolfsberg (ZCW) powder averaging scheme (at least 89 directions).

Frequency-Domain Fourier Transform THz-EPR Studies. Measurements were performed on crushed crystals of Mn_2Os·7MeOH (ca. 100 mg) on the THz beamline at the BESSY II storage ring (Berlin, Germany). The experimental setup is similar to that described previously.[82] The desolvated sample (Mn_2Os) was prepared by submitting the pristine crystalline sample to vacuum conditions ($p = 2 \times 10^{-6}$ mbar) for 3 h. Afterward, the sample was ground, mixed with Teflon, and pressed into a pellet.

Inelastic Neutron Scattering (INS). Measurements were performed on the cold neutron multidisc-chopper time-of-flight spectrometer TOFTOF at the Forschungs-Neutronenquelle Heinz Maier-Leibnitz (FRM II) (Garching, Germany). Approximately 900 mg of non-deuterated crystals of Mn_2Os·7MeOH were loaded into a 10 mm diameter double-walled aluminum cylinder which was sealed under a helium atmosphere. A standard closed-cycle refrigerator cryostat was used for the temperature control. Spectra were acquired with incident neutron wavelengths of 3 and 4.5 Å at temperatures between 3.4 and 40 K. The data were reduced and analyzed using the Large Array Manipulation Program (LAMP).[94]

Numerical Simulations Involving INS and THz-EPR Data. INS and THz-EPR spectra as well as magnetic susceptibility $\chi(T)$ and magnetization $M(H)$ curves obtained for Mn_2Os·7MeOH were calculated in addition being simulated from the magnetic data. Calculations were performed based on full diagonalization using a home-written MATLAB code. Directional averaging was achieved by employing a 110-point Lebedev−Laikov grid.[95] The matrix representations of the extended Stevens operators were generated using the *stev* function from the EasySpin software package.[96] The following Hamiltonian, enhanced by the tensorial notation of the single-ion

DOI: 10.1021/jacs.5b09378
J. Am. Chem. Soc. 2015, 137, 14406−14422

Table 1. Crystal Structural Data and Refinement Parameters for Single Crystals of Mn_2Fe·7MeOH, Mn_2Ru·7MeOH, Mn_2Os·7MeOH, Mn_2Co·7MeOH, and Mn_2Co/Os·7MeOH Collected at Low Temperature

formula	$Mn_2FeC_{91}H_{94}N_{11}O_{13}P_2$ (Mn_2Fe·7MeOH)	$Mn_2RuC_{91}H_{93}N_{11}O_{13}P_2$ (Mn_2Ru·7MeOH)	$Mn_2OsC_{91}H_{93}N_{11}O_{13}P_2$ (Mn_2Os·7MeOH)	$Mn_2CoC_{91}H_{94}N_{11}O_{13}P_2$ (Mn_2Co·7MeOH)	$Mn_2Co_{0.92}Os_{0.08}C_{91}H_{94}N_{11}O_{13}P_2$ (Mn_2Co/Os·7MeOH)
space group	$C2/c$	$C2/c$	$C2/c$	$C2/c$	$C2/c$
unit cell	a = 17.033(2) Å	a = 17.190(7) Å	a = 17.170(2) Å	a = 17.047(4) Å	a = 17.062(1) Å
	b = 13.819(2) Å	b = 13.844(6) Å	b = 13.842(2) Å	b = 13.851(3) Å	b = 13.837(1) Å
	c = 37.129(5) Å	c = 37.28(2) Å	c = 37.158(5) Å	c = 37.202(8) Å	c = 37.104(2) Å
	β = 102.650(2)°	β = 102.757(6)°	β = 102.787(2)°	β = 102.585(2)°	β = 102.588(1)°
volume, V, Å^3	8527.4(19)	8655(6)	8612.1(19)	8573(3)	8549.2(9)
Z	4	4	4	4	4
density, ρ_{calc}, g/cm^3	1.385	1.398	1.474	1.380	1.392
abs. coeff., μ, mm^{-1}	0.567	0.566	1.867	0.589	0.693
crystal description	brown-red plate	brown-red needle	brown-red plate	red plate	red plate
crystal size, mm^3	0.44 × 0.34 × 0.05	0.15 × 0.05 × 0.02	0.60 × 0.35 × 0.06	0.14 × 0.09 × 0.03	0.16 × 0.14 × 0.04
data/parameters/restraints	9975/697/9	7291/564/4	9843/569/5	7318/571/0	7875/608/0
R [$F_0 > 4\sigma(F_0)$][a]	R_1 = 0.0356	R_1 = 0.0715	R_1 = 0.0257	R_1 = 0.0416	R_1 = 0.0347
	wR_2 = 0.0942	wR_2 = 0.1729	wR_2 = 0.0652	wR_2 = 0.1017	wR_2 = 0.0837
GOF on F^2	1.043	1.042	1.116	1.029	1.021
max/min residual density, e·Å^{-3}	0.739, −0.362	0.823, −0.823	1.082, −0.550	0.517, −0.318	0.628, −0.466
reflections collected	48 250 [R_{int} = 0.0267]	21 755 [R_{int} = 0.0593]	48 107 [R_{int} = 0.0374]	29 991 [R_{int} = 0.0731]	42 524 [R_{int} = 0.0471]
completeness	0.992	0.980	0.995	0.996	0.997

[a] $R_1 = \Sigma[|F_0| - |F_c|]/\Sigma|F_0|$; $wR_2 = \{\Sigma[w(F_0^2 - F_c^2)^2/\Sigma[w(F_0^2)^2]\}^{1/2}$; $w = 1/[\sigma^2F_0^2 + (g_1P)^2 + g_2P]$; $P = (F_0^2 + 2F_c^2)/3$; g_1, g_2 = SHELXL weighting parameters.

J. Am. Chem. Soc. 2015, 137, 14406−14422
DOI: 10.1021/jacs.5b09378

anisotropy and exchange coupling with respect to eq 1, was considered:

$$\hat{H} = \sum_{i=1,3} \hat{\mathbf{S}}_i \cdot \mathbf{D}_{\mathrm{Mn}} \cdot \hat{\mathbf{S}}_i - \hat{\boldsymbol{\tau}} \cdot 2\mathbf{J} \cdot (\hat{\mathbf{S}}_1 + \hat{\mathbf{S}}_3) + \mu_B \mu_0 \sum_{i=1,2,3} g_i \hat{\mathbf{S}}_i \cdot \mathbf{H} \tag{4}$$

The i index counts the metal ions in the trinuclear Mn(i = 1)−Os(i = 2)−Mn(i = 3) unit. The Os^{III} ion is described by a pseudospin τ = 1/2, while S = 2 applies for the Mn^{III} ions. The exchange coupling is given by the matrix $\mathbf{J}$ which is assumed to be diagonal with diagonal elements J_{xx}, J_{yy}, J_{zz}. The Mn single-ion magnetic anisotropy is given by the tensor $\mathbf{D}_{\mathrm{Mn}} = \mathbf{R}\mathbf{D}'\mathbf{R}^{-1}$ with $\mathbf{R} = \mathbf{r}_z(\theta)\,\mathbf{r}_x(\alpha)$ and $\mathbf{D}'$ = diag(−1/3D, −1/3D, 2/3D). The matrices $\mathbf{r}_x(\alpha)$ and $\mathbf{r}_z(\theta)$ denote the rotations about the x-axis and z-axis by an angle of α and θ degrees, respectively. The x, y, z axes are approximately collinear with the CN ligands of the Os^{III} ion. In an idealized geometry, the Mn^{III} ions are located in a tetragonally elongated octahedral environment. The ligand-field of the Os^{III} ion is approximated to be perfectly octahedral.

In this idealized geometry, the angles of the Mn^{III} magnetic anisotropy tensors $\mathbf{D}_{\mathrm{Mn}}$ are determined to be α = 45° and θ = 49.3°. In the calculations of the magnetic susceptibility, a weak intermolecular magnetic coupling was taken into account by a mean field approach, characterized by a mean-field constant λ given by

$$\chi_{\mathrm{MF}} = \frac{1}{3} \sum_{i=x,y,z} \left[\frac{1}{\chi_{\mathrm{calc},i}} - \lambda \right]^{-1} \tag{5}$$

Moreover, a temperature-independent paramagnetism of $\chi_{\mathrm{TIP}} = 5 \times 10^{-4}$ cm^3/mol of the Os^{III} ion was taken into account. The least-squares fits were performed by minimizing the sum of squared deviations:

$$\kappa^2 = \frac{1}{N} \sum_k {w_k}^2 \frac{(y_{\mathrm{obs},k} - y_{\mathrm{calc},k})^2}{{\delta_k}^2} \tag{6}$$

δ_k and w_k are factors corresponding to the experimental error and an additional weight, respectively. N is the number of observations. The factors w_k were used to balance the influence of the spectroscopic peaks (w_k = 5) with respect to that of the $\chi(T)$ observations. For the latter ones, w_k were set to 1. The magnetization data was not used as observations.

RESULTS AND DISCUSSION

Syntheses. Single crystals of all reported compounds were obtained by reacting $[Mn^{III}(salphen)(H_2O)][ClO_4]\cdot 2H_2O$ with $(PPN)_3[M^{III}(CN)_6]\cdot H_2O$ (where M = Co, Fe, Ru, Os, Co/Os and PPN = bis(triphenylphosphoranylidene)ammonium) in approximately a 1.5:1 molar ratio in methanol. The self-assembly reaction results in molecules that are stable in air, but when removed from the mother liquor, loss of interstitial solvent occurs, eliciting a change in the observed magnetic properties. To ensure a complete removal of interstitial solvent, the pristine compounds $Mn_2Os\cdot 7MeOH$, $Mn_2Ru\cdot 7MeOH$, $Mn_2Fe\cdot 7MeOH$, $Mn_2Co\cdot 7MeOH$, and $Mn_2Co/Os\cdot 7MeOH$ were subjected to vacuum (ca. 1 mbar) for ca. 5 h to obtain the desolvated compounds: Mn_2Os, Mn_2Ru, Mn_2Fe, Mn_2Co, and Mn_2Co/Os. Crystals of all compounds can be stored in sealed vessels at −20 °C without decomposition for more than 6 months, but when left at room temperature in the mother liquor the compounds produce brown MnO_2 after few weeks. The desolvated compounds are stable only when stored under an inert gas atmosphere or vacuum due to their hygroscopic nature.

X-ray Crystallographic Studies. Single crystals of all five compounds were subjected to X-ray diffraction studies and were found to be isostructural with the following molecular formula: (PPN) $\{[Mn(salphen)(MeOH)]_2[M(CN)_6]\}\cdot 7MeOH$ (M = Os, Ru, Fe, Co, Co/Os for $Mn_2Os\cdot 7MeOH$, $Mn_2Ru\cdot 7MeOH$, $Mn_2Fe\cdot 7MeOH$, $Mn_2Co\cdot 7MeOH$ and $Mn_2Co/Os\cdot 7MeOH$, respectively). The molecules crystallize in the monoclinic $C2/c$ space group and their structures consist of anionic cyano-bridged trinuclear units, $\{[Mn(salphen)(MeOH)]_2[M(CN)_6]\}^-$, and PPN^+ cations (Figure 2 and Figure S1). Each

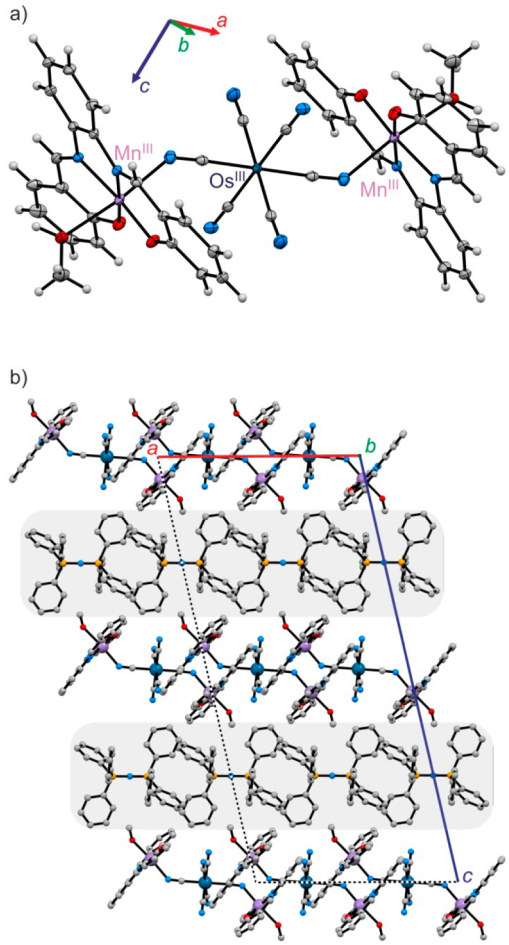

Figure 2. (a) $\{[Mn(salphen)(MeOH)]_2[Os(CN)_6]\}^-$ anion in $Mn_2Os\cdot 7MeOH$ (with thermal ellipsoids at 50% probability level). Os, dark blue; Mn, magenta; N, blue; O, red; C, gray. (b) Ball-and-stick representation of the crystal packing in the *ac*-plane showing the alternating layers of trinuclear complexes and PPN cations (highlighted in gray). Hydrogen atoms and crystallization solvent were omitted for the sake of clarity.

trinuclear unit is composed of a central hexacyanometallate anion bound to two $\{Mn(salphen)(MeOH)\}^+$ complex cations through *trans* bridging cyanide ligands to give an overall negative charge. Given the isostructural character of all reported compounds, only the structure of $Mn_2Os\cdot 7MeOH$ will be described in detail as it is representative of the family. Asymmetric units for all five compounds are provided in Figure S1 in the Supporting Information.

As illustrated for $Mn_2Os\cdot 7MeOH$ depicted in Figure 2a, the Mn^{III} centers are bound through the nitrogen atoms of *trans*-cyanide groups to the central $[Os^{III}(CN)_6]$ unit. The Mn−N(1) distance is 2.228(2) Å, and the Mn−N(1)−C(1) angle is significantly bent at 136.4(2)°. While such a low angle is atypical for most cyanide bridged complexes, it is well

DOI: 10.1021/jacs.5b09378
J. Am. Chem. Soc. 2015, 137, 14406−14422

documented for other reported trinuclear species in the C{[Mn(salen-type ligand)(solv)]$_2$[M(CN)$_6$]} (C = cation) family,[77−82] including the recently reported Os^{III} and Ru^{III} analogues with $\{Mn^{III}(5\text{-Brsalen})\}^+$ capping units.[82] The coordination environment of the Mn^{III} ions is that of an axially elongated octahedron in which the equatorial plane is occupied by the N_2O_2 donor atoms of the salphen ligand (average Mn-X distance of 1.93 Å), one of the two apical sites is occupied by a nitrogen atom N1 of the cyanide group of $[Os^{III}(CN)_6]^{3-}$ (bond length of 2.228(2) Å) and the remaining site is occupied by an oxygen atom of the coordinating methanol molecule (bond length of 2.312(2) Å; Table S1). The Jahn−Teller elongation axis of Mn^{III} ions in each molecule is parallel, although not perfectly, to its long direction. A packing diagram projected onto the *ac*-plane (Figure 2b) for Mn_2Os·7MeOH depicts the layer-like arrangement of the trinuclear Mn_2Os complexes separated by layers of PPN^+ cations.

A closer inspection of the crystal packing reveals intermolecular interactions that result in a 2-D supramolecular layered arrangement of the molecules. Specifically, there are $\pi-\pi$ interactions between the *o*-phenylenediimine rings of the nearest neighbor {Mn(salphen)(MeOH)} moieties (closest contacts = 3.365 and 3.417 Å typical of aromatic face-to-face $\pi-\pi$ stacking; Figure 3),[97,98] and hydrogen bonds between the axial MeOH ligand, the interstitial MeOH molecule and a terminal CN group (Figure 3b) which lead to a chain of H-bonds with the following D···A distances: $O_{MeOH}\cdots O_{MeOH}$ of 2.675 Å and $O_{MeOH}\cdots N_{CN}$ of 2.739 Å. The 2-D supramolecular layers of Mn−Os−Mn molecules are therefore stabilized by $\pi-\pi$ stacking that propagates along the *a* direction and H-bonding that propagates along the [110] direction. Additional details of the structures of the other trinuclear molecules: Mn_2Ru·7MeOH, Mn_2Fe·7MeOH, Mn_2Co·7MeOH and Mn_2Co/Os·7MeOH are deposited in the Supporting Information (bond lengths and angles: Table S2, asymmetric units: Figure S1, packing diagram with MeOH included: Figure S2).

Crystals of all five compounds lose interstitial solvent molecules very readily as already mentioned. Unfortunately, the structural changes could not be followed by diffraction techniques due to the significant loss of crystallinity upon desolvation. Surprisingly, however, the desolvation process is completely reversible as demonstrated for Mn_2Os·7MeOH by performing a series of PXRD experiments after two subsequent desolvation/resolvation cycles (Figure 4). The resolvated form does not retain the single crystal form, but its powder diffraction pattern is nearly identical to that of the pristine sample with only slight broadening of the diffraction peaks. Each compound was desolvated/resolvated several times to confirm the persistent character of the observed "solvent dependent" properties.

Magnetic Studies. Magnetic properties of Mn_2Co·7MeOH and its desolvated form Mn_2Co containing the diamagnetic central Co^{III} ion will be discussed first as these data provide important information about the intrinsic properties of the peripheral Mn^{III} ions in the series (g_{Mn} factor, zero-field splitting parameter D_{Mn}, and intramolecular magnetic exchange constant J_{MnMn}; $H = -2J_{MnMn}S_{Mn1}S_{Mn2}$) crucial for understanding the more complex behavior of Mn_2Os·7MeOH, Mn_2Ru·7MeOH, and Mn_2Fe·7MeOH.

DC Magnetic Properties of Mn_2Co·7MeOH and Mn_2Co. The χT vs T plot of pristine Mn_2Co·7MeOH is presented in Figure 5 together with M vs H (inset) data. The χT values remain roughly constant down to 20 K

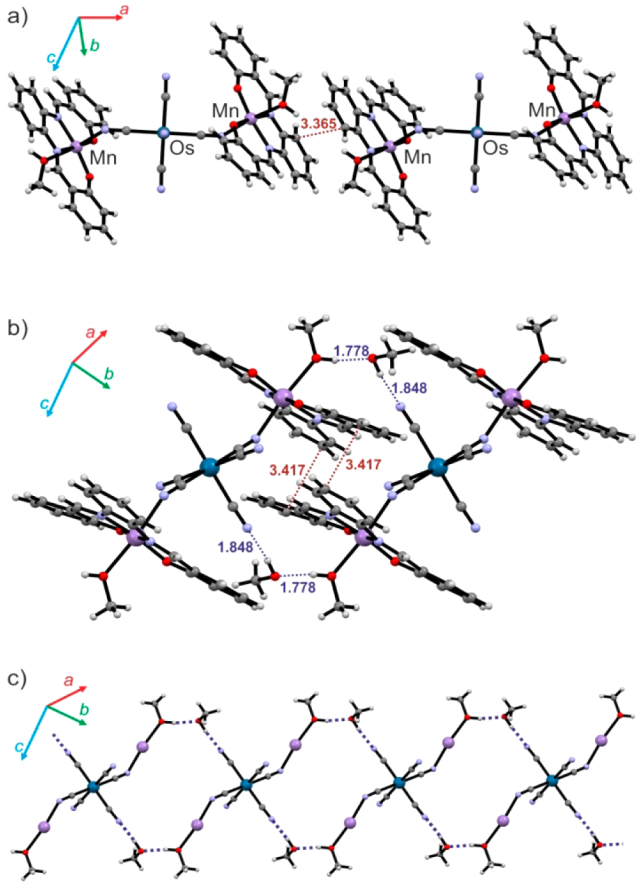

Figure 3. Ball-and-stick view of the $\pi-\pi$ stacking interactions between the "phen" rings of the salphen ligand (a), $\pi-\pi$ stacking interactions between "sal" rings of the salphen ligand (b), and hydrogen bonds between the MeOH molecule of crystallization and the two adjacent Mn−Os−Mn molecules leading to supramolecular chain (c). Os, dark blue; Mn, magenta; N, blue; O, red; C, gray; H, white. In panel (c), salphen ligands are omitted for the sake of clarity.

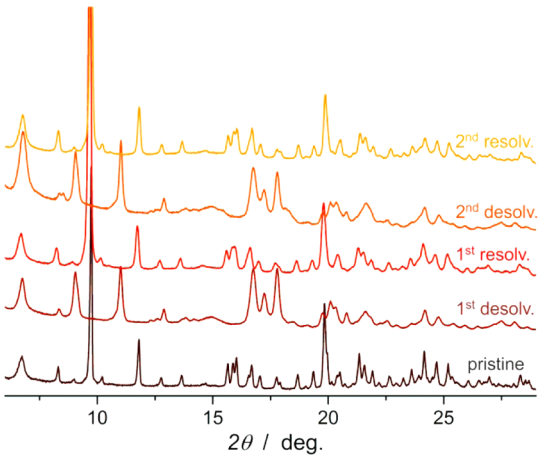

Figure 4. Room temperature experimental PXRD patterns for Mn_2Os·7MeOH after two consecutive desolvation/resolvation cycles.

beginning at 6.6 emu·K·mol^{-1} at room temperature which is in very good agreement with the spin only value of 6.0 emu·K·mol^{-1} expected for two noninteracting Mn^{III} centers ($S = 2$) assuming $g = 2.0$. Below 20 K, the χT product decreases significantly, reaching the lowest value at 1.8 K indicating

DOI: 10.1021/jacs.5b09378
J. Am. Chem. Soc. 2015, 137, 14406−14422

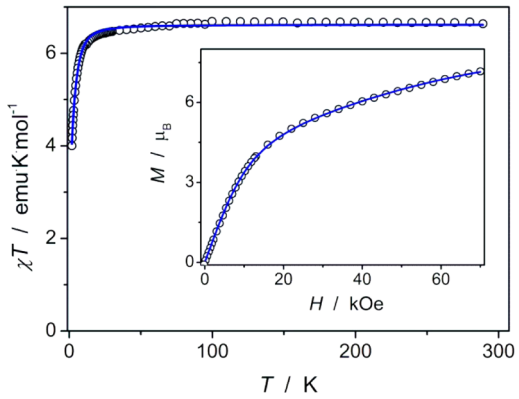

Figure 5. Plot of χT vs T under H_{DC} = 1000 Oe (main) and M vs H at 1.8 K (inset) for Mn_2Co·7MeOH (black circles, experimental data; blue lines, best fit for two antiferromagnetically interacting Mn^{III} centers; for details, see the text).

significant magnetic anisotropy and/or weak intramolecular antiferromagnetic interactions through the diamagnetic $[Co^{III}(CN)_6]^{3-}$ bridge. The best fit for two weakly interacting Mn^{III} centers (S = 2) results in the following parameters: g_{Mn} = 2.1(1), D_{Mn} = −3.5(1) cm^{-1}, and J_{MnMn} = −0.03(1) cm^{-1}. The field dependence of the magnetization (Figure 5 inset) shows a behavior typical for a paramagnet with a significant magnetic anisotropy. The best fit to the experimental data results in parameters that are consistent with those obtained from fitting the susceptibility data: g_{Mn} = 2.1(1), D_{Mn} = −3.7(1) cm^{-1}, and J_{MnMn} = −0.04(1) cm^{-1}. The magnetic anisotropy is further evidenced by the nonoverlapping isofield lines in the reduced magnetization plot in the 10−70 kOe and 1.8−5.4 K range. The best fit to the M vs HT^{-1} dependence yields parameters g_{Mn} = 2.1(1), D_{Mn} = −3.2(1) cm^{-1}, and J_{MnMn} = −0.04(1) cm^{-1}, similar to those obtained from χT vs T (Figure S3 in the Supporting Information).

The desolvation of Mn_2Co·7MeOH has a minimal effect on the DC magnetic properties. Similar to the pristine form, the χT product for Mn_2Co remains constant down to 20 K beginning at 6.6 emu·K·mol^{-1} at room temperature and decreases below 20 K reaching the lowest value at 1.8 K (Figure S4 in the Supporting Information). The best fit for two weakly interacting Mn^{III} centers (S = 2) results in the following parameters: g_{Mn} = 2.1(1), D_{Mn} = −3.1(1) cm^{-1}, and J_{MnMn} = −0.05(1) cm^{-1} which are comparable to those obtained for Mn_2Co·7MeOH (vide supra). The field dependence of the magnetization (Figure S4 inset) also exhibits behavior typical of a paramagnet with significant magnetic anisotropy. The best fit to the experimental data results in parameters that are comparable with those obtained from fitting the susceptibility data: g_{Mn} = 2.2(1), D_{Mn} = −2.7(1) cm^{-1}, and J_{MnMn} = −0.04(1) cm^{-1}.

DC Magnetic Properties of Mn_2M·7MeOH and the Mn_2M Families (M = Os^{III}, Ru^{III}, Fe^{III}). The magnetic properties for Mn_2Os·7MeOH and Mn_2Os will be discussed as the representative ones. The magnetic data for Mn_2Ru·7MeOH, Mn_2Ru, Mn_2Fe·7MeOH and Mn_2Fe are presented in parentheses and in Table 2 and in additional figures. The χT vs T data of the pristine Mn_2Os·7MeOH are shown in Figure 6 (Figures 7 and 8 for Mn_2Ru·7MeOH and Mn_2Fe·7MeOH, respectively; triangles). The χT product is 6.6 emu·K·mol^{-1} at room temperature (Mn_2Ru·7MeOH, 6.8 emu·K·mol^{-1};

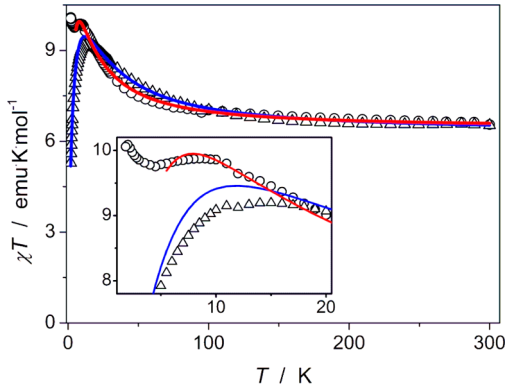

Figure 6. χT vs T under H_{DC} = 1000 Oe for Mn_2Os·7MeOH (triangles, experimental data; blue line, best fit) and Mn_2Os (circles, experimental data; red line, best fit). For details, see the text.

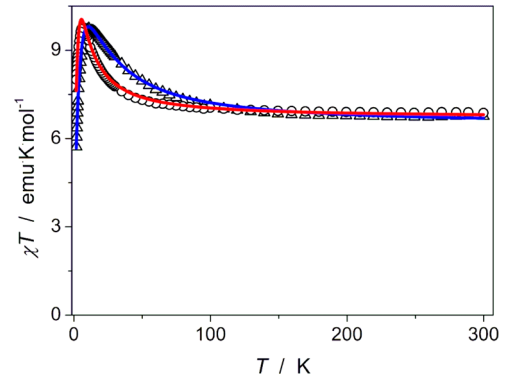

Figure 7. χT vs T under H_{DC} = 1000 Oe for Mn_2Ru·7MeOH (triangles, experimental data; blue line, best fit) and Mn_2Ru (circles, experimental data; red line, best fit). For details, see the text.

Table 2. Comparison of the Experimental χT Values and the Fitting Parameters Obtained from the DC Magnetic Susceptibility Data of the Mn_2M·7MeOH and Mn_2M Families (M = Co, Os, Ru, Fe) Including the Temperature of the Maximum of the $\chi T(T)$ plot, $T[(\chi T)_{max}]$

	$(\chi T)_{RT}$/cm^3 K mol^{-1}	$(\chi T)_{max}$/cm^3 K mol^{-1}	$T[(\chi T)_{max}]$/K	g_{Mn}	g_{effM}	D_{Mn}/cm^{-1}	J_{MnM}/cm^{-1}	zJ'/cm^{-1}
Mn_2Co·7MeOH	6.6			2.1(1)		−3.5(1)	−0.03(1)[a]	
Mn_2Co	6.6			2.1(1)		−3.1(1)	−0.05(1)[a]	
Mn_2Os·7MeOH	6.6	9.2	13.0	2.0[b]	1.75[b]	−3.5[b]	+9.7(2)	−0.09(1)
Mn_2Os	6.7	9.9	9.0	2.0[b]	1.75[b]	−3.1[b]	+7.7(1)	−0.04(1)
Mn_2Ru·7MeOH	6.8	9.7	11.0	2.0[b]	1.88[b]	−3.5[b]	+9.7(1)	−0.07(1)
Mn_2Ru	6.9	9.8	6.5	2.05[b]	1.88[b]	−3.1[b]	+4.0(1)	−0.03(1)
Mn_2Fe·7MeOH	6.7	10.6	9.0	2.05[b]	1.98[b]	−3.5[b]	+5.9(2)	−0.05(1)
Mn_2Fe	6.5	10.1	6.0	2.0[b]	1.98[b]	−3.1[b]	+4.5(1)	−0.02(1)

[a] J_{MnMn}. [b] Fixed parameters.

DOI: 10.1021/jacs.5b09378
J. Am. Chem. Soc. 2015, 137, 14406−14422

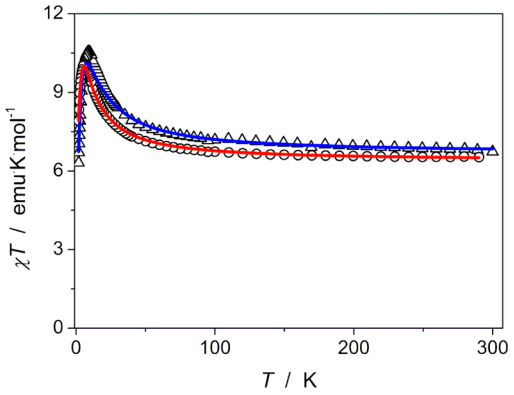

Figure 8. χT vs T under H_{DC} = 1000 Oe for Mn_2Fe·7MeOH (triangles, experimental data; blue line, best fit) and Mn_2Fe (circles, experimental data; red line, best fit). For details, see the text.

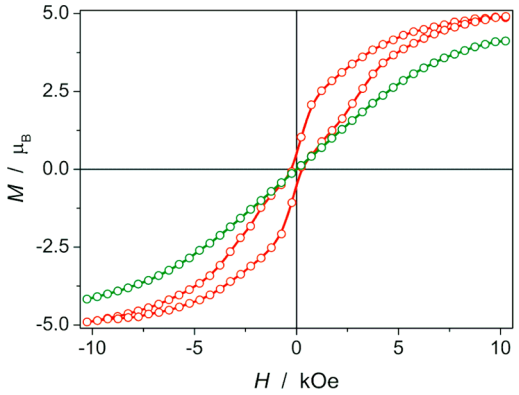

Figure 9. M vs H hysteresis loops for Mn_2Os·7MeOH (green) and Mn_2Os (red) measured at 1.8 K with 0.031 kOe/s magnetic field average sweep rate. Solid lines are merely guides for the eye.

Mn_2Fe·7MeOH, 6.7 emu·K·mol^{-1}) which is slightly lower than the spin-only value 7.0 emu·K·mol^{-1} for two Mn^{III} g = 2.1 and one Os^{III} g = 2.0 ion. The χT remains roughly constant down to 200 K and then increases slowly to reach a maximum of 9.2 emu·K·mol^{-1} at 13 K (Mn_2Ru·7MeOH: 9.7 emu·K·mol^{-1} at 11 K; Mn_2Fe·7MeOH: 10.6 emu·K·mol^{-1} at 9 K) indicating the presence of significant intramolecular ferromagnetic interactions between Mn and Os centers. Below 12.9 K the value decreases abruptly to 5.3 emu·K·mol^{-1} at 1.8 K due to the zero-field splitting, strong spin−orbit coupling, and also possibly weak intermolecular antiferromagnetic interactions (Mn_2Ru·7MeOH, 5.7 emu·K·mol^{-1}; Mn_2Fe·7MeOH, 6.3 emu·K·mol^{-1}).

An attempt to fit the magnetic susceptibility data for Mn_2Os·7MeOH over the 1.8−300 K range was made using eqs 1 and 2 assuming g_{Mn} = 2.0, g_{effOs} = 1.75, D_{Mn} = −3.5 cm^{-1} and allowing J_{MnOs} and zJ' to vary (fitting parameters for Mn_2Ru·7MeOH and Mn_2Fe·7MeOH are summarized in Table 2). The best fit with J_{MnOs} = +9.7(2) cm^{-1} and zJ' = −0.09(1) cm^{-1} is shown as the blue solid line in Figure 6 (Figures 7 and 8 for Mn_2Ru·7MeOH and Mn_2Fe·7MeOH, respectively) and is in good agreement with the observed magnetic behavior of Mn_2Os·7MeOH (Mn_2Ru·7MeOH, J_{MnRu} = +9.7(1) cm^{-1}, zJ' = −0.07(1) cm^{-1}; Mn_2Fe·7MeOH, J_{MnFe} = +5.9(2) cm^{-1}, zJ' = −0.05(1) cm^{-1}). The field dependence of the magnetization measured at 1.8 and 4.0 K (Figure S5 in the Supporting Information, and Figures S6 and S7 for Mn_2Ru·7MeOH and Mn_2Fe·7MeOH, respectively, at 1.8 K) revealed an abrupt increase of the magnetization at low magnetic fields and a steady increase without obvious saturation at 70 kOe. Such magnetic field behavior is clearly indicative of a magnetic ground state with significant anisotropy. Simulation of the magnetization curves using the set of parameters obtained from the fitting the magnetic susceptibility data qualitatively reproduces the experimental results. Fast magnetization measurements at 1.8 K with the 0.031 kOe/s average magnetic field sweep rate did not reveal any signature of magnetic hysteresis (green points in Figure 9).

The desolvation process for the Mn_2Os·7MeOH sample has an obvious impact on the magnetic susceptibility in the low temperature range. At high temperatures (above 40 K), the χT vs T plot for Mn_2Os shown in Figure 6 (Figures 7 and 8 for Mn_2Ru and Mn_2Fe, respectively; circles) looks very similar to that of Mn_2Os·7MeOH with a χT product of 6.7 emu·K·mol^{-1} at room temperature. Below 40 K, however, the χT value exhibits a round maximum of 9.9 emu·K·mol^{-1} at a slightly lower temperature of 9.0 K indicating weaker intramolecular ferromagnetic interactions than what is observed for Mn_2Os·7MeOH (Mn_2Ru and Mn_2Fe behave similarly). Additionally, the χT product increases below 5 K reaching 10.1 emu·K·mol^{-1} at 1.8 K which is in direct contrast to Mn_2Os·7MeOH. This peculiar behavior will be explained in the following section along with a discussion of the AC magnetic properties. Fitting of the magnetic susceptibility of Mn_2Os was carried out with nearly the same set of parameters as for Mn_2Os·7MeOH in the 5.5−300 K temperature range with only D_{Mn} being different at −3.1(1) cm^{-1} (fitting parameters and the results for Mn_2Ru and Mn_2Fe are shown in Table 2). The best fit shown as the red solid line in Figure 6 (Figures 7 and 8 for Mn_2Ru and Mn_2Fe, respectively) is in excellent agreement with the observed magnetic behavior above 5.5 K with J_{MnOs} = +7.7(1) cm^{-1} and zJ' = −0.04(1) cm^{-1} (Mn_2Ru, J_{MnRu} = +4.0(1) cm^{-1} and zJ' = −0.03(1) cm^{-1}; Mn_2Fe, J_{MnFe} = +4.5(1) cm^{-1} and zJ' = −0.02(1) cm^{-1}). It is worth noting that the absolute values of the intramolecular exchange and the mean-field constants decrease significantly upon desolvation of Mn_2Os·7MeOH (the same trend is observed for Mn_2Ru·7MeOH and Mn_2Fe·7MeOH). The field dependence of the magnetization data measured at 1.8 and 4.0 K for Mn_2Os (Figure S8 in the Supporting Information and Figures S9 and S10 for Mn_2Ru and Mn_2Fe, respectively) shows an increase of the magnetization at low magnetic fields that is even more abrupt than in the case of Mn_2Os·7MeOH. As the field increases, a steady increase occurs without clear saturation at 70 kOe. Such behavior is also indicative of a magnetic ground state with significant anisotropy. Simulation of the magnetization curves using the set of parameters obtained from the fitting of the χT vs T plot is in good qualitative agreement with the experimental data. Interestingly, fast magnetization measurements at 1.8 K with a 0.031 kOe/s average magnetic field sweep rate exhibits a "waist-restricted" magnetic hysteresis loop (red points in Figure 9) with a coercive field of H_{cr} = 800 Oe.

It is important to emphasize that desolvation of Mn_2Os·7MeOH and Mn_2Ru·7MeOH is completely reversible and that the magnetic susceptibilities of the solvated and desolvated compounds overlap almost perfectly after two full desolvation/resolvation cycles (Figures S11 and S12 in the Supporting Information).

DC Magnetic Properties of Mn_2Co/Os·7MeOH and Mn_2Co/Os. In order to better appreciate the role of the central

DOI: 10.1021/jacs.5b09378
J. Am. Chem. Soc. 2015, 137, 14406−14422

metal ion in the reported trinuclear SMMs and the relevance of the inter- and/or intramolecular interactions in the magnetization relaxation changes, a partially magnetically diluted system with an approximate 9:1 Co:Os metal ratio, (PPN)-{[Mn^{III}(salphen)]$_2$[$Co^{III}_{0.92}Os^{III}_{0.08}(CN)_6$]}·7MeOH ($Mn_2Co$/Os·7MeOH) and its desolvated form Mn_2Co/Os were prepared. The intended result of the magnetic dilution of Mn_2Os with Mn_2Co was to quench the intermolecular interactions between the Mn_2Os molecules (through the central metal ion) by separating them with Mn_2Co complexes. The DC magnetic properties of Mn_2Co/Os·7MeOH and Mn_2Co/Os are dominated by the properties of Mn_2Co molecules as shown in Figure S13 (Supporting Information). However, after subtracting the contribution of the Mn_2Co·7MeOH and Mn_2Co (92%, based on the previously discussed experimental results on these pure complexes), the remaining magnetic susceptibility in the form of χT vs T dependence is similar to that of the pure (i.e., nondiluted) Mn_2Os·7MeOH and Mn_2Os, respectively (Figure 10). The χT vs T plot for Mn_2Co/Os·7MeOH

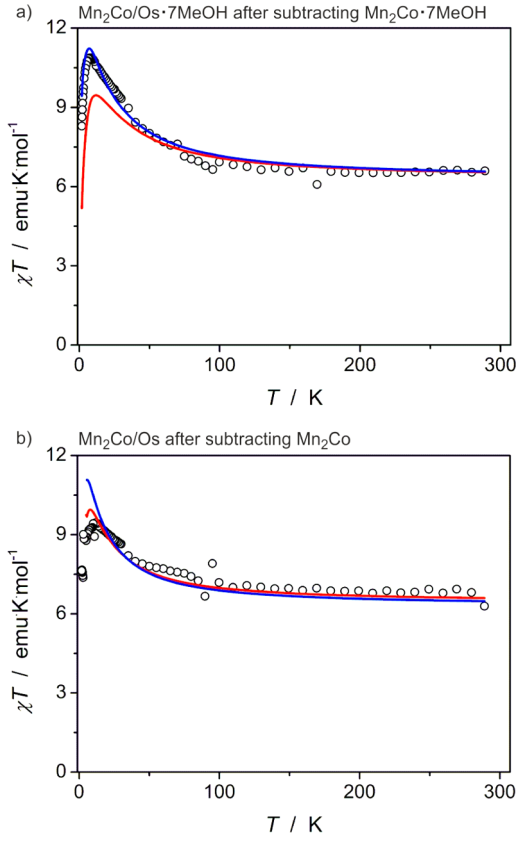

Figure 10. Plot of χT vs T (black circles) for Mn_2Co/Os·7MeOH (a) and Mn_2Co/Os (b) after subtracting the contribution of Mn_2Co using the experimental data for Mn_2Co·7MeOH and Mn_2Co, respectively. The red line is the best simulation for Mn_2Os·7MeOH including intermolecular interactions zJ' (as in Figure 6) and the blue line is a second simulation of the Mn_2Os·7MeOH susceptibility in absence of intermolecular interactions zJ'.

after subtracting the contribution of Mn_2Co molecules (Figure 10a) is in good agreement with the simulated magnetic behavior of Mn_2Os·7MeOH with the aforementioned parameters (vide supra) in the absence of intermolecular interactions. This result suggests that the dilution does indeed quench the intermolecular interactions between Mn_2Os molecules. A qualitatively similar conclusion can be drawn in the case of the desolvated Mn_2Co/Os (Figure 10b).

Summary of the DC Data for the Mn_2M Family. Analyses of the magnetic properties of the family of trinuclear molecules Mn_2M in both pristine and desolvated form are consistent with the conclusion that the intramolecular coupling constant J_{MnM} decreases when the central ion M is being replaced with a lighter element congener (Table 2).

Moreover, in each case, the desolvation weakens the intra- as well as intermolecular interactions. Weakening of the intermolecular interactions can be understood on the basis of destroying the hydrogen bonding network upon removal of interstitial MeOH molecules (hydrogen bonds are known to transmit magnetic interactions on the order of the estimated zJ' values[60] or even stronger[99]) and the PPN^+ cations rearrangement resulting in a better separation of the Mn_2M molecules. The structural changes upon desolvation may also cause changes in the M-CN-Mn bridges (Figure S14 in the Supporting Information) which could explain the change in the strength of the ferromagnetic interactions J_{MnM}.

Results of the Detailed Study of Mn_2Os·7MeOH by Inelastic Neutron Scattering and THz-EPR Spectroscopy. It has been demonstrated that the use of isotropic or Ising-type exchange coupling in the modeling of the magnetic properties of $[Os^{III}(CN)_6]^{3-}$ based cyanide-bridged complexes is often a risky approximation and that anisotropic exchange coupling should be used instead.[82] In order to obtain a deeper insight into the magnetic model for Mn_2Os·7MeOH, inelastic neutron scattering (INS) and frequency-domain Fourier-transform terahertz electron paramagnetic resonance spectroscopy (THz-EPR)[100] have been used in combination with SQUID magnetometry in order to determine the anisotropic exchange constants between Mn^{III} and Os^{III} magnetic sites. INS and THz-EPR spectra of Mn_2Os·7MeOH are shown in Figure 11. The low temperature (3.4 and 3.8 K) INS spectra reveal two prominent energy loss peaks at 14.1 and 35 cm^{-1}. When heating to 20 K the intensity of this peak decreases as expected for a magnetic ground state excitation. This assignment is corroborated by spectra measured at 40 K (Figures S15 and S16) and by the linear momentum transfer (Q) dependence revealing that the peak intensities are constant or decreasing with increasing Q (Figure S17). In addition, the phonon background is well estimated by scaling the 40 K spectrum (Figure S15c) by the Bose population factor[101] $[1 - \exp(-\hbar\omega/k_BT)]^{-1}$ as shown by the gray line in Figure 11 (and Figures S15 and S16). In the 20 K spectra, two peaks at ~6 and ~8.5 cm^{-1} appear which were not present at the lower temperatures. These features can be assigned to magnetic transitions from the first excited state to other excited states in view of their Q dependence as shown in Figure S17. For the THz-EPR spectra of Mn_2Os·7MeOH, two features are observed at 11.5 and 14.1 cm^{-1} (Figure 11), where only the latter is ascribed to a magnetic ground state excitation after examination of their dependence on magnetic field and temperature (Figure S18). In Figure 11, the peaks are labeled Mi and mi denoting transitions from the ground state or from an excited state, respectively.

The THz-EPR spectra of the desolvated Mn_2Os exhibit a single feature at 20.6 cm^{-1} (green trace in Figure 11). Its dependence on magnetic field and temperature (Figure S19) indicates that it is a magnetic ground state excitation. The first fitting attempt using an isotropic exchange coupling was performed, and the best fit results are plotted in Figure S15. The χT vs T product could be successfully reproduced, but the

DOI: 10.1021/jacs.5b09378
J. Am. Chem. Soc. 2015, 137, 14406−14422

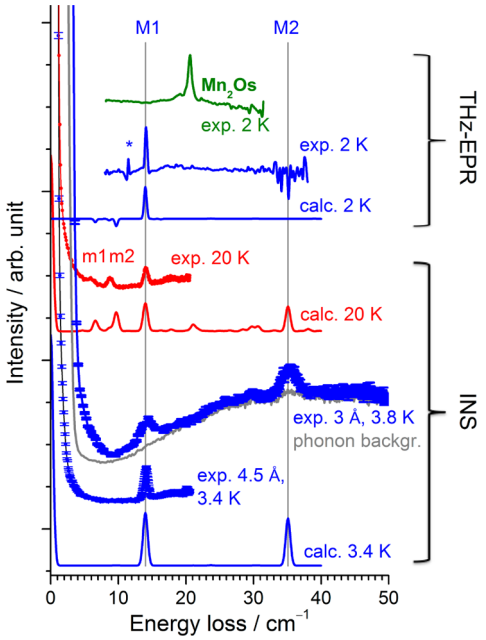

Figure 11. Experimental and calculated THz-EPR and INS spectra of Mn_2Os·7MeOH (except the green trace which is Mn_2Os) obtained at temperatures as indicated in the plot. Neutron wavelengths are given in Angstroms. The gray line indicates the estimated phonon background as described in the text. Spectra have been offset for clarity.

spectroscopy results do not match as well. Also, the best fit value of the ZFS parameter for Mn^{III} centers $D = -5.6$ cm^{-1} appears to be slightly high. The other best fit parameter values are reasonable: $J_{iso} = +10.8$ cm^{-1} ($H = -2J_{12}S_1S_2$ formalism), $\lambda = -0.150$ mol emu^{-1}, $g_1 = g_3 = 1.98$, and $g_2 = 1.8$. Note that the exchange coupling strength obtained with the use of additional data from INS and THz-EPR spectra is very similar to that obtained exclusively from the DC magnetic susceptibility as demonstrated in Table 2.

To improve the agreement with the spectroscopic data, the constraint of isotropic exchange was released and different J_{xx}, J_{yy}, J_{zz} were allowed. The INS and THz-EPR spectra as well as the χT vs T data were fitted as described in the Experimental Details section. In these fits, five parameters were allowed to vary freely: the three $J_{\beta\beta}$ values as well as D and λ keeping $g_1 = g_3 = 1.98$ and $g_2 = 1.8$. As a result three sets of parameters were obtained that led to an excellent reproduction of the experimental data. The three sets (Table 3) have one common feature: for each set, one $J_{\beta\beta}$ is positive (ferromagnetic). Fit "X" gives the best match with the data but since fits "Y" and "Z" are almost as good, it is difficult to determine with certainty which of the $J_{\beta\beta}$ should be positive. The best fits of INS, THz-EPR and χT vs T are plotted in Figures 11 and S16, demonstrating excellent agreement with the experimental data. In a previous study of a related Mn−Os−Mn SMM,[82] the presence of a ferromagnetic and two antiferromagnetic $J_{\beta\beta}$ values was found, similar to the findings on Mn_2Os·7MeOH shown here. However, the average coupling strength $J_{av} = (|J_{xx}| + |J_{yy}| + |J_{zz}|)/3$ in Mn_2Os·7MeOH is $J_{av} = 25.8$ cm^{-1} which is almost a factor of 2 larger than $J_{av}' = 14.3$ cm^{-1} found in ref 82 (taking into account the 2J and 1J formalisms, respectively).

Remarkably, the comparison of THz-EPR spectra of Mn_2Os·7MeOH and Mn_2Os reveals that the zero-field splitting (zfs) has increased by 150% upon desolvation. This correlates well

Table 3. Best Fit Parameters for Mn_2Os·7MeOH Using All Available Data and the Anisotropic Exchange Approach As Described in the Main Text

	fit X	fit Y	fit Z
J_{xx}/cm^{-1}	+30.0(5)	−25.5(5)	−22.0(5)
J_{yy}/cm^{-1}	−23.5(5)	+32.0(5)	−25.9(2)
J_{zz}/cm^{-1}	−24.0(5)	−24.0(5)	+28.9(2)
D_{Mn}/cm^{-1}	−4.1(1)	−4.2(1)	−3.7(1)
λ/mol·emu^{-1}	−0.074(4)	−0.070(4)	−0.073(4)
κ^{2a}	4.1	4.6	4.7

[a]Sum of squared deviations.

with the increase of the effective barrier of 240% obtained from AC susceptibility measurements described below. The discrepancy may be due to a difference in wave functions which determine the QTM rate between different Kramers doublets. The narrow line width (fwhm = 0.6 cm^{-1}) of the THz-EPR feature at 20.6 cm^{-1} is in accord with the rather low distribution parameter α of the relaxation time (Table S3).

AC Magnetic Properties of Mn_2Os·7MeOH and Mn_2Os. Given that the family of compounds of general type $(C)\{[Mn(L)(solv)]_2[M(CN)_6]\}$ (C = cation, solv = solvent, M = Cr^{III}, Fe^{III}, Ru^{III}, Os^{III})[77−82,87,102] are known to exhibit SMM behavior, the AC magnetic susceptibility measurements for all reported compounds were performed to probe the magnetization dynamics. AC magnetic susceptibilities of Mn_2Os·7MeOH and Mn_2Os exhibit an obvious frequency dependence, typical of SMMs under a zero DC field with a single relaxation mode (Figures 12 and S20). Cole−Cole plots (χ'' vs χ' plots; Figure S21 in the Supporting Information) for both compounds were fitted using the following equation from the generalized Debye model for a single relaxation process with a distribution (α) of relaxation times (τ):[103]

$$\chi'' = \left\{ \frac{(\chi_0' - \chi_\infty')^2 \tan^2(\alpha\pi/2)}{4} + [(\chi_0' - \chi_\infty')(\chi' - \chi_\infty') - (\chi' - \chi_\infty')^2] \right\}^{1/2} - \frac{(\chi_0' - \chi_\infty')}{2} \tan\left(\frac{\alpha\pi}{2}\right) \quad (7)$$

In this generalized Debye model approach, the in-phase and out-of-phase AC susceptibility can be expressed as follows:

$$\chi' = \chi_\infty' + \frac{(\chi_0' - \chi_\infty')\left[1 + (2\pi\nu\tau)^{1-\alpha} \sin\left(\frac{\alpha\pi}{2}\right)\right]}{1 + 2(2\pi\nu\tau)^{1-\alpha} \sin\left(\frac{\alpha\pi}{2}\right) + (2\pi\nu\tau)^{2(1-\alpha)}} \quad (8)$$

$$\chi'' = \frac{(\chi_0' - \chi_\infty')(2\pi\nu\tau)^{1-\alpha} \cos\left(\frac{\alpha\pi}{2}\right)}{1 + 2(2\pi\nu\tau)^{1-\alpha} \sin\left(\frac{\alpha\pi}{2}\right) + (2\pi\nu\tau)^{2(1-\alpha)}} \quad (9)$$

The temperature dependence of the AC magnetic susceptibilities is shown in Figure S22. Selected data, including τ and α obtained from the fits of the Cole−Cole plots of Mn_2Os·7MeOH and Mn_2Os using eq 7 are summarized in Table S3. The effective energy barrier (U_{eff}/k_B) of the magnetization reversal of 17.1 K (Mn_2Os·7MeOH) and 42.0 K (Mn_2Os) were obtained by fitting the ln(τ) vs T^{-1} plot to the Arrhenius law (Figure 12), $\tau = \tau_0 \exp(U_{eff}/k_BT)$, in the 1.8−3.3 K ($Mn_2Os$·7MeOH) and 2.5−4.5 K ($Mn_2Os$) temperature ranges. The attempt times of relaxation (τ_0) of 3.96×10^{-7} s

DOI: 10.1021/jacs.5b09378
J. Am. Chem. Soc. 2015, 137, 14406−14422

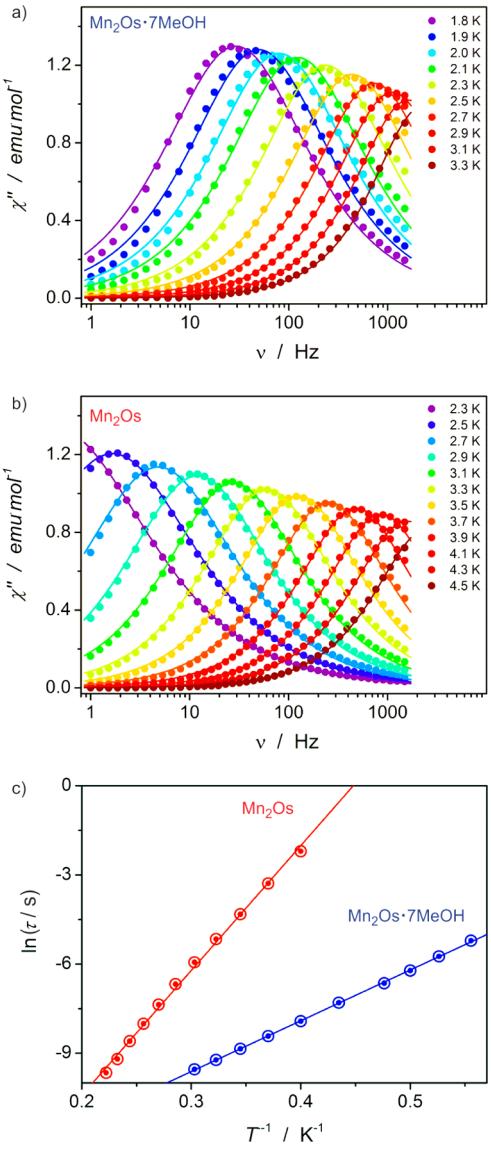

Figure 12. Out-of-phase AC magnetic susceptibility vs frequency data under a zero DC field for Mn_2Os·7MeOH (a) and Mn_2Os (b) (solid lines are the best fits to the generalized Debye model; eq 9) with Arrhenius plot (c) for Mn_2Os·7MeOH (blue) and Mn_2Os (red) (solid lines are the best fits to the Arrhenius law using the experimental data indicated with filled symbols).

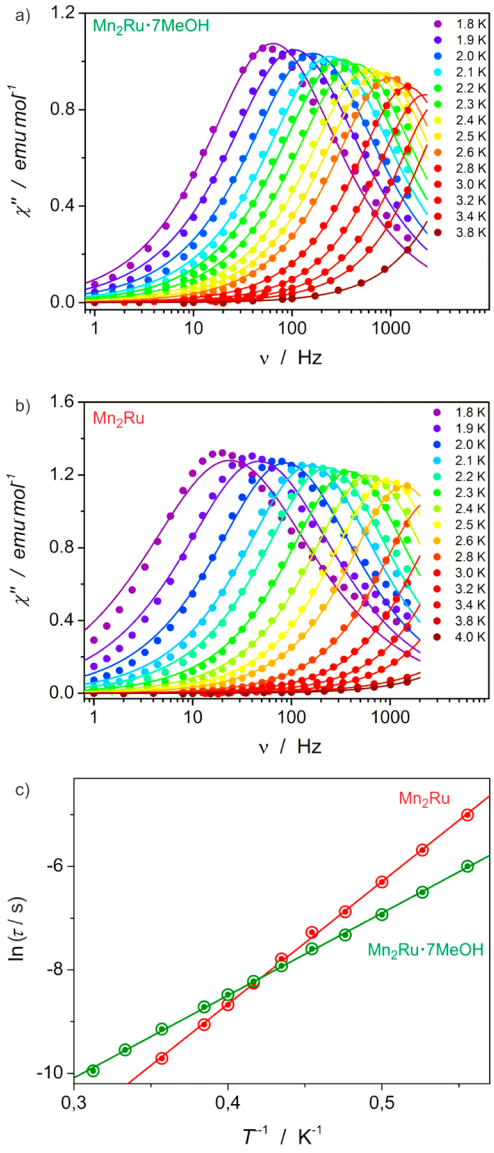

Figure 13. Out-of-phase AC magnetic susceptibility vs frequency data under zero DC field for Mn_2Ru·7MeOH (a) and Mn_2Ru (b) (solid lines are the best fits to the generalized Debye model; eq 9) with Arrhenius plot (c) for Mn_2Ru·7MeOH (green) and Mn_2Ru (red) (solid lines are the best fits to the Arrhenius law using experimental data indicated with filled symbols).

(Mn_2Os·7MeOH) and 6.69×10^{-9} s (Mn_2Os) are within the limits typical for SMMs.

It is worth noting that, upon desolvation, the energy barrier increases by a factor of 2.4 to the value of 42.0 K which is close to 58.3 K, the highest energy barrier ever reported for a cyanide-bridged SMM.[46] These energy barriers and the respective SMM properties are fully reversible as demonstrated by the temperature dependence of the AC magnetic susceptibility measured at three different frequencies after three complete desolvation/resolvation cycles (Figure S23 depicts the almost ideal overlap of the out-of-phase AC signal for the solvated and desolvated samples, respectively).

AC Magnetic Properties of Mn_2Ru·7MeOH and Mn_2Ru. AC magnetic susceptibilities of Mn_2Ru·7MeOH and Mn_2Ru also exhibit a strong frequency dependence under zero DC field with a single relaxation mode similar to Mn_2Os·7MeOH and Mn_2Os but at slightly lower temperatures (Figures 13 and S24). Cole−Cole plots (Figure S25) for both compounds were fitted using eq 7. Selected data, including τ and α obtained from the fits, are summarized in Table S4. The effective energy barriers (U_{eff}/k_B) of the magnetization reversal of 15.9 K (Mn_2Ru·7MeOH) and 24.4 K (Mn_2Ru) were obtained by fitting the $\ln(\tau)$ vs T^{-1} plot to the Arrhenius law in the 1.8−3.2 K temperature range. The attempt time of relaxation (τ_0) of 3.50×10^{-7} s (Mn_2Ru·7MeOH) and 1.05×10^{-8} s (Mn_2Ru) are within the limits typical for SMMs. It is worth noting that desolvation leads to an increase in the SMM energy barrier of only a factor of 1.5 as compared to 2.4 for Mn_2Os analogous system. As was found for Mn_2Os·7MeOH/Mn_2Os, these energy barriers and the respective SMM properties of the Mn_2Ru·7MeOH/Mn_2Ru system are fully reversible as demonstrated by the temperature dependence of the AC magnetic susceptibility data measured at three different frequencies after two desolvation/resolvation cycles (Figure S26).

DOI: 10.1021/jacs.5b09378
J. Am. Chem. Soc. 2015, 137, 14406−14422

AC Magnetic Properties of Mn_2Fe·7MeOH and Mn_2Fe. Similarly to the Os and Ru analogues, AC magnetic susceptibilities of Mn_2Fe·7MeOH and Mn_2Fe also exhibit a strong frequency dependence under zero magnetic field with a single mode of magnetization relaxation at lower temperatures than previously described for the two other systems (Figures 14 and S27). Cole−Cole plots (Figure S28) for both compounds were fit using eq 7. Selected data, including τ and α obtained from the fits, are summarized in Table S5. The effective SMM energy barriers (U_{eff}/k_B) of 14.7 K (Mn_2Fe·7MeOH) and 22.2 K (Mn_2Fe) were obtained by fitting the $\ln(\tau)$ vs T^{-1} plots to the Arrhenius law in the 1.8−2.3 K (Mn_2Fe·7MeOH) and 1.8−3.3 K (Mn_2Fe) temperature ranges, respectively. The attempt times of relaxation (τ_0) of 8.02×10^{-8} s (Mn_2Fe·7MeOH) and 2.94×10^{-8} s (Mn_2Fe) are typical. It is worth noting that upon desolvation the energy barrier increases by the factor of 1.5−exactly in the same way as for the Mn_2Ru system and much lower as compared to 2.4 for the Mn_2Os analogue. The energy barrier and the SMM behavior of Mn_2Fe·7MeOH/Mn_2Fe are also fully reversible (Figure S29).

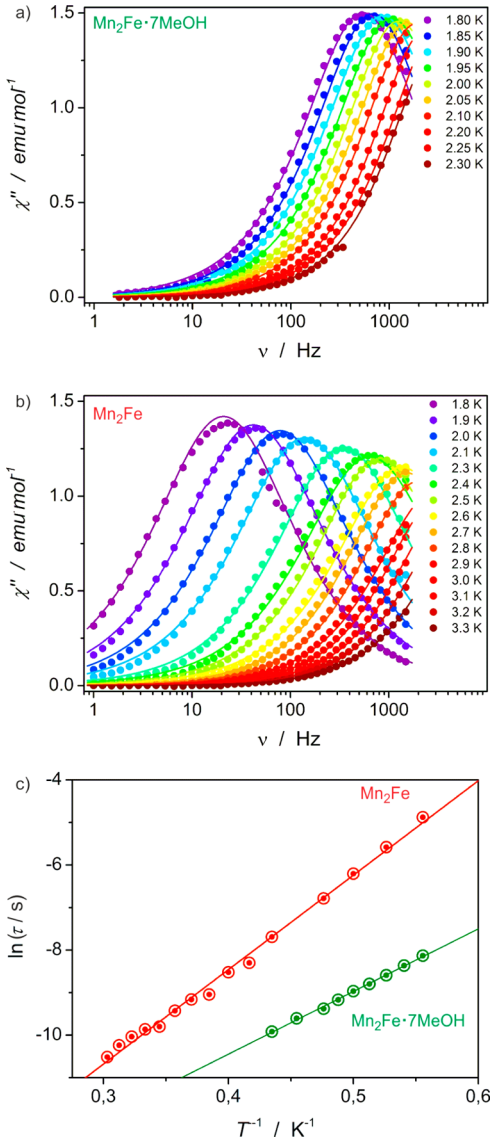

Figure 14. Out-of-phase AC magnetic susceptibility vs frequency under a zero DC field for Mn_2Fe·7MeOH (a) and Mn_2Fe (b) (solid lines are the best fits to the generalized Debye model; eq 9) with the Arrhenius plot (c) for Mn_2Fe·7MeOH (green) and Mn_2Fe (red) (solid lines are the best fits to the Arrhenius law using experimental data indicated with filled symbols).

AC Magnetic Properties of Mn_2Co·7MeOH and Mn_2Co. AC magnetic susceptibilities of Mn_2Co·7MeOH and Mn_2Co reveal a weak frequency dependence in the absence of a magnetic field (Figure S30) with more pronounced signals being observed under applied DC fields of 500 and 1400 Oe, respectively. Figure S31 shows the determination of the optimum fields for AC measurements, and Figure S32 depicts the frequency dependence of the in-phase and the out-of-phase signals. Cole−Cole plots (Figure S33 in the Supporting Information) for both compounds were fit using eq 7 in order to obtain the relaxation time values and to estimate the effective energy barriers from the Arrhenius law.

Selected Cole−Cole fitting parameters, including τ and α obtained from the fits are summarized in Table S6. The effective energy barriers (U_{eff}/k_B) of the magnetization reversal were estimated to be around 10 K (Mn_2Co·7MeOH) and 12 K (Mn_2Co) (see Arrhenius plot in Figure S34). Note that both values are only rough estimates. The attempt times of relaxation (τ_0) were estimated to be 4.9×10^{-8} s (Mn_2Co7·MeOH) and 7.2×10^{-6} s (Mn_2Co) which are usual values. In contrast to the other trinuclear analogues with paramagnetic central metal ions, there is basically no change in the SMM energy barrier upon desolvation of Mn_2Co·7MeOH. This underscores the importance of the identity of the central unit, not only for the energy barrier height, but also for the magnetization dynamics and suggests that it may have at least in part an intramolecular origin for Mn_2M molecules based on the paramagnetic central ion M.

AC Magnetic Properties of Mn_2Co/Os·7MeOH and Mn_2Co/Os. The diluted system was studied by AC magnetic susceptibility measurements in order to verify the influence of the quasi-diamagnetic dilution on the slow relaxation of the magnetization of Mn_2Os. The AC data for Mn_2Co/Os·7MeOH and Mn_2Co/Os reveal a strong frequency dependence of both the in-phase and out-of-phase components in the absence of an applied DC field (Figure 15) with pronounced maxima that can be assigned to Mn_2Os molecules and an onset of the out-of-phase signal in the high frequency region−assigned to Mn_2Co molecules which is only present at low temperatures for the both the pristine Mn_2Co/Os·7MeOH and the desolvated Mn_2Co/Os. For the sake of clarity, the Mn_2Co out-of-phase signal at 1.8, 1.9, and 2.0 K was removed from Figure 15a and b and was omitted during the fitting (see Figure S35 for the AC data before the removal of the Mn_2Co contribution). The χ'' vs ν data for Mn_2Co/Os·7MeOH and Mn_2Co/Os were fitted using a generalized Debye model for a single relaxation process with a distribution (α) of relaxation times (τ) using eq 9.[103] Please note that the χ' vs ν could not be fit due to the significant and inseparable contribution from the Mn_2Co molecules. Selected data, including τ and α obtained from the fits of the χ'' vs ν plots of Mn_2Co/Os·7MeOH and Mn_2Co/Os using eq 9 are summarized in Table S7. The effective energy barrier values (U_{eff}/k_B) of 15.3 K (Mn_2Co/Os·7MeOH) and 35.6 K (Mn_2Co/Os) were obtained by fitting the temperature dependence of the relaxation time to the Arrhenius law in the 2.8−3.2 K (Mn_2Co/Os·7MeOH) and 3.2−4.0 K (Mn_2Co/Os) temperature ranges. The energy barriers for Mn_2Os in the diluted Mn_2Co/Os·7MeOH and Mn_2Co/Os are similar to those for pure Mn_2Os·7MeOH and Mn_2Co/Os compounds

DOI: 10.1021/jacs.5b09378
J. Am. Chem. Soc. 2015, 137, 14406−14422

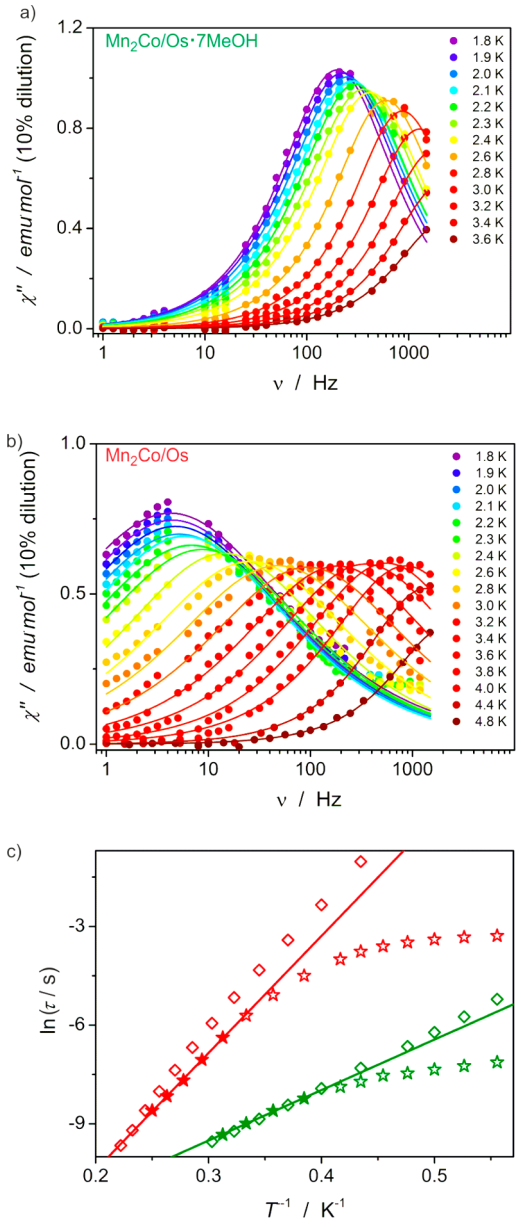

Figure 15. Out-of-phase AC magnetic susceptibility vs frequency under a zero DC field for $Mn_2Co/Os·7MeOH$ (a) and Mn_2Co/Os (b) accounting for the 10% magnetic dilution; solid lines are the best fits to eq 9. Arrhenius plots (c) for $Mn_2Co/Os·7MeOH$ (green stars), Mn_2Co/Os (red stars), $Mn_2Os·7MeOH$ (green diamonds), and Mn_2Os (red diamonds). Solid lines are the best fits to the Arrhenius law using the data indicated with filled symbols.

(17.1 and 42.0 K, respectively). It is worth noting that the desolvation of this diluted system also leads to an increase of the SMM energy barrier by a factor of 2.3 in a similar fashion to what was observed for the pure $Mn_2Os·7MeOH$ upon desolvation. In the low temperature range, the slow dynamics likely occurs by quantum tunneling of the magnetization (QTM). This situation is in contrast to the behavior observed for the nondiluted Mn_2Os.

Micro-SQUID Measurements on $Mn_2Os·7MeOH$ and Mn_2Os. To further explore the relaxation dynamics of the SMMs in this study, magnetic hysteresis loops were collected on easy-axis oriented single crystal samples using a micro-SQUID magnetometer. Magnetization measurements for $Mn_2Os·7MeOH$ revealed strongly temperature and field sweep rate dependent hysteretic behavior below 2.0 K (Figures 16 and S36).

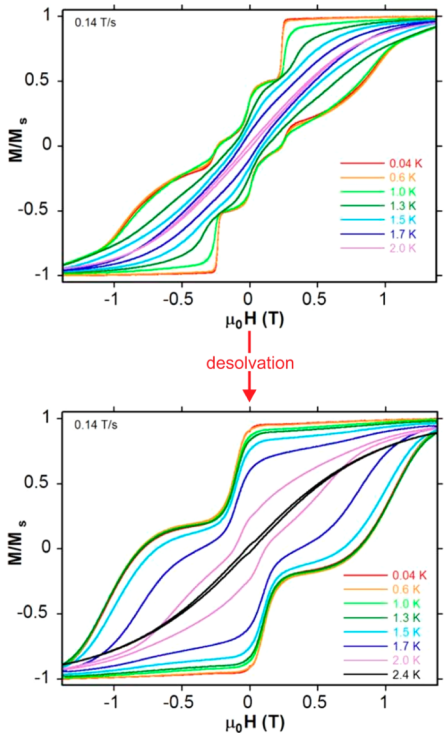

Figure 16. Field dependence of the magnetization on an easy-axis oriented crystal of $Mn_2Os·7MeOH$ (top) and Mn_2Os (bottom) at different temperatures with a field sweep rate of 0.14 T/s.

The first quantum tunneling step occurs at 0.25 T which suggests an exchange-bias behavior due to the weak intermolecular antiferromagnetic interactions between SMM complexes.[60−69]

For a single crystal of magnetically isolated SMMs, the first step in the hysteresis loop due to the quantum tunneling of the magnetization should occur at zero field (when the external field is oriented parallel to the easy axis of the crystal). If there are weak interactions between the adjacent SMMs, however, a shift of the first tunneling step occurs as an indication of exchange bias a situation first reported for the $[Mn_4]_2$ dimer of SMMs based on $[Mn_4O_3Cl_4(O_2CEt)_3(py)_3]_2$,[62] with subsequent examples being reported in the past few years.[60−69] Surprisingly the strong sweep rate dependence of the two-step hysteresis loops measured for $Mn_2Os·7MeOH$ is observed even at 40 mK (Figure S36). This magnetization properties are similar to the steps reported by Lecren et al. for the 1D arrangement of exchange coupled $[Mn_2(salpn)_2(H_2O)_2]^{2+}$ SMMs[104] and suggests that $Mn_2Os·7MeOH$ is a system of exchange biased SMMs. Conversely, the micro-SQUID measurements for Mn_2Os are typical of SMM behavior without significant intermolecular exchange interactions (Figure 16), an observation that is consistent with the DC data. These results support the conclusion that a weakening of the intermolecular interactions occurs upon desolvation (Figure 6). The hysteresis loop (Figure 16) revealed only one magnetization step for Mn_2Os close to zero-DC field that corresponds to the fast quantum tunneling relaxation between the two lower-energy levels, $m_S = \pm 9/2$.[61] As in the case of $Mn_2Os·7MeOH$, the

DOI: 10.1021/jacs.5b09378
J. Am. Chem. Soc. 2015, 137, 14406−14422

hysteresis loops for Mn_2Os show a very strong magnetic field sweep rate dependence even at 40 mK (Figure S36).

Summary of the SMM Behavior of Mn_2M Family. In this section, the modulation of the SMM behavior will be discussed only for the Mn_2Os case but the conclusions are also valid for the Fe and Ru analogues. The Arrhenius plots in Figure 15c summarize the temperature dependence of the relaxation times at different temperatures for the undiluted (diamonds) and diluted (stars) for the Mn_2Os compounds in the pristine (green) and desolvated (red) state. At "high" temperatures, the behavior of $Mn_2Co/Os{\cdot}7MeOH$ and Mn_2Co/Os is linear (i.e., mainly thermally activated) and very similar to $Mn_2Os{\cdot}7MeOH$ and Mn_2Os, respectively. Significant deviations from linearity are only observed below 2.2 and 2.6 K, respectively, when the quantum relaxation pathway becomes progressively dominant. These observations strongly suggest that in the investigated temperature range (above 1.8 K) the changes in the intermolecular interactions upon desolvation of $Mn_2Os{\cdot}7MeOH$ cannot be the main cause of the SMM energy barrier modification as it has basically the same effect on the diluted phase $Mn_2Co/Os{\cdot}7MeOH$ (which has a quasi-absence of intermolecular interactions). These facts also exclude the possibility that the SMM behavior is being switched to Single Chain Magnet (SCM) behavior upon desolvation or vice versa (at least above 1.8 K) as one might be tempted to hypothesize from the crystal structure (compare Figures 3c and S14). Quenching of the intermolecular interactions by diluting Mn_2Os in the Mn_2Co matrix, however, may be responsible for the deviation of the experimental data from the Arrhenius law at low temperatures (Figure 15c) due to the quantum tunneling of magnetization. In the absence of intermolecular interactions, the quantum tunneling of the magnetization becomes a dominant relaxation pathway for $Mn_2Co/Os{\cdot}7MeOH$ and Mn_2Co/Os at low temperatures and in a zero DC field.

With all the aforementioned data taken together, a reasonable conclusion is that the observed modification of the SMM energy barrier must originate from a change in the geometry of the trinuclear complex—most likely a change in the CN bridge angles as shown in Figure S14 (the middle one). In view of the observed anisotropic exchange interactions, a more linear Os—CN—Mn geometry is expected to lead to improved alignment of the local magnetic anisotropy axes of Mn^{III} and $[Os^{III}(CN)_6]^{3-}$[81] which should have a strong impact on the strength and sign of the Mn—Os anisotropic exchange couplings. Therefore, we conclude that the origin of the change of the magnetization dynamics upon desolvation is most likely due to *intramolecular* rather than *intermolecular* effects. By generalizing this approach, more deliberate geometrical control of the Os—CN—M angle could provide a unique possibility for obtaining SMMs with a large and tunable energy barriers.

CONCLUSIONS

A detailed study of four new SMMs, namely, $(PPN)\{[Mn^{III}(salphen)(MeOH)]_2[M^{III}(CN)_6]\}{\cdot}7MeOH$ ($Mn_2M{\cdot}7MeOH$) (M = Fe, Ru, Os and Co) and a mixed metal Co/Os analogue $(PPN)\{[Mn^{III}(salphen)(MeOH)]_2[Co^{III}_{0.92}Os^{III}_{0.08}(CN)_6]\}{\cdot}7MeOH$, revealed that the energy barriers for magnetization reversal increase significantly when the central atom is replaced by a heavier congener. The results lend further credence to the contention that SMM properties can be significantly improved by the use of heavy d-block metal centers with unquenched orbital angular momentum and strong spin—orbit coupling which lead to anisotropic magnetic exchange interactions.

Additionally, it was demonstrated that the energy barriers of Mn_2Fe, Mn_2Ru, and Mn_2Os trinuclear complexes can be reversibly switched by desolvation/resolvation of the respective crystalline phases. The energy barrier for Mn_2Os reaches 42.0 K after desolvation, which is one of the highest energy barriers ever reported for a cyanide-bridged SMM. Remarkably, modification of the magnetization dynamics is completely reversible and can be repeated many times without any sign of decomposition. The magnetic dilution of the Mn_2Os SMM in a paramagnetic Mn_2Co matrix revealed that the alteration of the SMM energy barrier originally observed in the pristine $Mn_2Os{\cdot}7MeOH$ is preserved in the diluted $Mn_2Co/Os{\cdot}7MeOH$ analog despite the considerable weakening of intermolecular interactions. This strongly suggests that the difference in the magnetization dynamics for the whole series is of intramolecular origin and most likely induced by a structural change of the M—CN—Mn geometry as a consequence of the disruption of the supramolecular H-bonding interactions upon desolvation as well as possible changes in the packing of the cations. INS and THz-EPR measurements confirm that the desolvation-induced structural alterations impact the anisotropic exchange interactions leading to the observed switchable SMM behavior.

Finally, during the course of these studies, it was also observed that $Mn_2Os{\cdot}7MeOH$ exhibits exchange-bias SMM behavior in contrast to typical SMM properties exhibited by Mn_2Os after desolvation. The $Mn_2Os{\cdot}7MeOH$ compound appears to be the first example of a cyanide-bridged SMM exhibiting the exchange-bias phenomenon and related quantum physics (tunneling shift) that can be controlled by guest molecules.

ASSOCIATED CONTENT

Supporting Information

The Supporting Information is available free of charge on the ACS Publications website at DOI: 10.1021/jacs.5b09378.

Additional structural diagrams, crystallographic data, magnetic plots, and fitting results (PDF)
Crystallographic data for $Mn_2Co{\cdot}7MeOH$ (CIF)
Crystallographic data for $Mn_2CoOs{\cdot}7MeOH$ (CIF)
Crystallographic data for $Mn_2Fe{\cdot}7MeOH$ (CIF)
Crystallographic data for $Mn_2Fe{\cdot}7MeOH\_RT$ (CIF)
Crystallographic data for $Mn_2Os{\cdot}7MeOH$ (CIF)
Crystallographic data for $PPN_3Os(CN)_6$ (CIF)
Crystallographic data for $Mn_2Os{\cdot}7MeOH\_RT$ (CIF)
Crystallographic data for $PPN_3Ru(CN)_6$ (CIF)
Crystallographic data for $Mn_2Ru{\cdot}7MeOH$ (CIF)
Crystallographic data for Mn_3Co (CIF)

AUTHOR INFORMATION

Corresponding Authors

*dunbar@chem.tamu.edu
*dawid.pinkowicz@uj.edu.pl, pinkowic@chemia.uj.edu.pl

Notes

The authors declare no competing financial interest.

ACKNOWLEDGMENTS

This material is based on work at Texas A&M University supported by the U.S. Department of Energy, Materials Sciences Division, under Grant Nos. DE-FG02-02ER45999

DOI: 10.1021/jacs.5b09378
J. Am. Chem. Soc. 2015, 137, 14406—14422

and DE-SC0012582. D.P. acknowledges the financial support of the Polish Ministry of Science and Higher Education, within the Iuventus Plus Programme (Grant Agreement No. 0370/IP3/2015/73). This work was also supported by the Centre National de la Recherche Scientifique (CNRS), the University of Bordeaux, and the Conseil Regional d'Aquitaine. K.S.P. thanks The Danish Research Council for a DFF | Sapere Aude: Research Talent award (Grant 4090-00201). J.D. acknowledges financial support from the Swiss National Science Foundation, Grant No. PZ00P2_142474. This project has received funding from the European Union's Seventh Framework Programme for research, technological development and demonstration under the NMI3-II Grant Number 283883 for the INS studies.

REFERENCES

(1) Caneschi, A.; Gatteschi, D.; Sessoli, R.; Barra, A. L.; Brunel, L. C.; Guillot, M. *J. Am. Chem. Soc.* **1991**, *113*, 5873.
(2) Aubin, S. M. J.; Wemple, M. W.; Adams, D. M.; Tsai, H.-L.; Christou, G.; Hendrickson, D. N. *J. Am. Chem. Soc.* **1996**, *118*, 7746.
(3) Christou, G.; Gatteschi, D.; Hendrickson, D. N.; Sessoli, R. *MRS Bull.* **2000**, *25*, 66.
(4) Gatteschi, D.; Sessoli, R. *Angew. Chem., Int. Ed.* **2003**, *42*, 268.
(5) Thomas, L.; Lionti, F.; Ballou, R.; Gatteschi, D.; Sessoli, R.; Barbara, B. *Nature* **1996**, *383*, 145.
(6) Wernsdorfer, W.; Sessoli, R. *Science* **1999**, *284*, 133.
(7) Barbara, B.; Thomas, L.; Lionti, F.; Chiorescu, I.; Sulpice, A. *J. Magn. Magn. Mater.* **1999**, *200*, 167.
(8) Coronado, E.; Galán-Mascarós, J.-R.; Gómez-García, C.-J.; Ensling, J.; Gütlich, P. *Chem. - Eur. J.* **2000**, *6*, 552.
(9) Boudalis, A. K.; Donnadieu, B.; Nastopoulos, V.; Clemente-Juan, J. M.; Mari, A.; Sanakis, Y.; Tuchagues, J.-P.; Perlepes, S. P. *Angew. Chem., Int. Ed.* **2004**, *43*, 2266.
(10) Wittick, L. M.; Murray, K. S.; Moubaraki, B.; Batten, S. R.; Spiccia, L.; Berry, K. J. *Dalton Trans.* **2004**, 1003.
(11) Foguet-Albiol, D.; O'Brien, T. A.; Wernsdorfer, W.; Moulton, B.; Zaworotko, M. J.; Abboud, K. A.; Christou, G. *Angew. Chem., Int. Ed.* **2005**, *44*, 897.
(12) Koizumi, S.; Nihei, M.; Nakano, M.; Oshio, H. *Inorg. Chem.* **2005**, *44*, 1208.
(13) Cornia, A.; Fabretti, A. C.; Garrisi, P.; Mortalò, C.; Bonacchi, D.; Gatteschi, D.; Sessoli, R.; Sorace, L.; Wernsdorfer, W.; Barra, A.-L. *Angew. Chem., Int. Ed.* **2004**, *43*, 1136.
(14) Milios, C. J.; Inglis, R.; Vinslava, A.; Bagai, R.; Wernsdorfer, W.; Parsons, S.; Perlepes, S. P.; Christou, G.; Brechin, E. K. *J. Am. Chem. Soc.* **2007**, *129*, 12505.
(15) Gregoli, L.; Danieli, C.; Barra, A.-L.; Neugebauer, P.; Pellegrino, G.; Poneti, G.; Sessoli, R.; Cornia, A. *Chem. - Eur. J.* **2009**, *15*, 6456.
(16) Tasiopoulos, A. J.; Perlepes, S. P. *Dalton Trans.* **2008**, 5537.
(17) Pedersen, K. S.; Bendix, J.; Clerac, R. *Chem. Commun.* **2014**, *50*, 4396.
(18) Sessoli, R.; Gatteschi, D.; Caneschi, A.; Novak, M. A. *Nature* **1993**, *365*, 141.
(19) Sessoli, R.; Tsai, H. L.; Schake, A. R.; Wang, S.; Vincent, J. B.; Folting, K.; Gatteschi, D.; Christou, G.; Hendrickson, D. N. *J. Am. Chem. Soc.* **1993**, *115*, 1804.
(20) Christou, G. *Polyhedron* **2005**, *24*, 2065.
(21) Lis, T. *Acta Crystallogr., Sect. B: Struct. Crystallogr. Cryst. Chem.* **1980**, *36*, 2042.
(22) Ako, A. M.; Hewitt, I. J.; Mereacre, V.; Clérac, R.; Wernsdorfer, W.; Anson, C. E.; Powell, A. K. *Angew. Chem., Int. Ed.* **2006**, *45*, 4926.
(23) Murugesu, M.; Takahashi, S.; Wilson, A.; Abboud, K. A.; Wernsdorfer, W.; Hill, S.; Christou, G. *Inorg. Chem.* **2008**, *47*, 9459.
(24) Tasiopoulos, A. J.; Vinslava, A.; Wernsdorfer, W.; Abboud, K. A.; Christou, G. *Angew. Chem., Int. Ed.* **2004**, *43*, 2117.
(25) Waldmann, O. *Inorg. Chem.* **2007**, *46*, 10035.
(26) Ruiz, E.; Cirera, J.; Cano, J.; Alvarez, S.; Loose, C.; Kortus, J. *Chem. Commun.* **2008**, 52.
(27) Zadrozny, J. M.; Atanasov, M.; Bryan, A. M.; Lin, C.-Y.; Rekken, B. D.; Power, P. P.; Neese, F.; Long, J. R. *Chem. Sci.* **2013**, *4*, 125.
(28) Zadrozny, J. M.; Long, J. R. *J. Am. Chem. Soc.* **2011**, *133*, 20732.
(29) Zhu, Y.-Y.; Cui, C.; Zhang, Y.-Q.; Jia, J.-H.; Guo, X.; Gao, C.; Qian, K.; Jiang, S.-D.; Wang, B.-W.; Wang, Z.-M.; Gao, S. *Chem. Sci.* **2013**, *4*, 1802.
(30) Vallejo, J.; Castro, I.; Ruiz-García, R.; Cano, J.; Julve, M.; Lloret, F.; De Munno, G.; Wernsdorfer, W.; Pardo, E. *J. Am. Chem. Soc.* **2012**, *134*, 15704.
(31) Ruamps, R.; Maurice, R.; Batchelor, L.; Boggio-Pasqua, M.; Guillot, R.; Barra, A. L.; Liu, J.; Bendeif, E.-E.; Pillet, S.; Hill, S.; Mallah, T.; Guihéry, N. *J. Am. Chem. Soc.* **2013**, *135*, 3017.
(32) Rinehart, J. D.; Long, J. R. *J. Am. Chem. Soc.* **2009**, *131*, 12558.
(33) Lin, P.-H.; Smythe, N. C.; Gorelsky, S. I.; Maguire, S.; Henson, N. J.; Korobkov, I.; Scott, B. L.; Gordon, J. C.; Baker, R. T.; Murugesu, M. *J. Am. Chem. Soc.* **2011**, *133*, 15806.
(34) Freedman, D. E.; Harman, W. H.; Harris, T. D.; Long, G. J.; Chang, C. J.; Long, J. R. *J. Am. Chem. Soc.* **2010**, *132*, 1224.
(35) Suzuki, K.; Sato, R.; Mizuno, N. *Chem. Sci.* **2013**, *4*, 596.
(36) Boulon, M.-E.; Cucinotta, G.; Luzon, J.; Degl'Innocenti, C.; Perfetti, M.; Bernot, K.; Calvez, G.; Caneschi, A.; Sessoli, R. *Angew. Chem., Int. Ed.* **2013**, *52*, 350.
(37) Coutinho, J. T.; Antunes, M. A.; Pereira, L. C. J.; Bolvin, H.; Marcalo, J.; Mazzanti, M.; Almeida, M. *Dalton Trans.* **2012**, *41*, 13568.
(38) Ishikawa, N.; Sugita, M.; Ishikawa, T.; Koshihara, S.-y.; Kaizu, Y. *J. Am. Chem. Soc.* **2003**, *125*, 8694.
(39) Pinkowicz, D.; Podgajny, R.; Nowicka, B.; Chorazy, S.; Reczynski, M.; Sieklucka, B. *Inorg. Chem. Front.* **2015**, *2*, 10.
(40) Brown, A. J.; Pinkowicz, D.; Saber, M. R.; Dunbar, K. R. *Angew. Chem., Int. Ed.* **2015**, *54*, 5864.
(41) Gómez-Coca, S.; Urtizberea, A.; Cremades, E.; Alonso, P. J.; Camón, A.; Ruiz, E.; Luis, F. *Nat. Commun.* **2014**, *5*, 4300.
(42) Fataftah, M. S.; Zadrozny, J. M.; Rogers, D. M.; Freedman, D. E. *Inorg. Chem.* **2014**, *53*, 10716.
(43) Zhu, Y.-Y.; Zhang, Y.-Q.; Yin, T.-T.; Gao, C.; Wang, B.-W.; Gao, S. *Inorg. Chem.* **2015**, *54*, 5475.
(44) Wang, X.-Y.; Avendano, C.; Dunbar, K. R. *Chem. Soc. Rev.* **2011**, *40*, 3213.
(45) Pinkowicz, D.; Southerland, H.; Wang, X.-Y.; Dunbar, K. R. *J. Am. Chem. Soc.* **2014**, *136*, 9922.
(46) Qian, K.; Huang, X.-C.; Zhou, C.; You, X.-Z.; Wang, X.-Y.; Dunbar, K. R. *J. Am. Chem. Soc.* **2013**, *135*, 13302.
(47) Dhers, S.; Costes, J.-P.; Guionneau, P.; Paulsen, C.; Vendier, L.; Sutter, J.-P. *Chem. Commun.* **2015**, *51*, 7875.
(48) Palii, A.; Ostrovsky, S. M.; Klokishner, S. I.; Tsukerblat, B. S.; Dunbar, K. R. *ChemPhysChem* **2006**, *7*, 871.
(49) Ostrovsky, S. M.; Klokishner, S. I.; Palii, A. V.; Dunbar, K. R. *J. Mol. Struct.* **2007**, *838*, 138.
(50) Palii, A. V.; Ostrovsky, S. M.; Klokishner, S. I.; Tsukerblat, B. S.; Schelter, E. J.; Prosvirin, A. V.; Dunbar, K. R. *Inorg. Chim. Acta* **2007**, *360*, 3915.
(51) Mironov, V. S. *Dokl. Phys. Chem.* **2007**, *415*, 199.
(52) Ruiz, E.; Rodríguez-Fortea, A.; Alvarez, S.; Verdaguer, M. *Chem. - Eur. J.* **2005**, *11*, 2135.
(53) Mironov, V. S.; Chibotaru, L. F.; Ceulemans, A. *J. Am. Chem. Soc.* **2003**, *125*, 9750.
(54) Mironov, V. *Dokl. Phys. Chem.* **2006**, *408*, 130.
(55) Ruiz, E.; Cirera, J.; Cano, J.; Alvarez, S.; Loose, C.; Kortus, J. *Chem. Commun.* **2008**, 52.
(56) Freedman, D. E.; Jenkins, D. M.; Iavarone, A. T.; Long, J. R. *J. Am. Chem. Soc.* **2008**, *130*, 2884.
(57) Sokol, J. J.; Hee, A. G.; Long, J. R. *J. Am. Chem. Soc.* **2002**, *124*, 7656.
(58) Schelter, E. J.; Prosvirin, A. V.; Dunbar, K. R. *J. Am. Chem. Soc.* **2004**, *126*, 15004.
(59) Schelter, E. J.; Karadas, F.; Avendaño, C.; Prosvirin, A. V.; Wernsdorfer, W.; Dunbar, K. R. *J. Am. Chem. Soc.* **2007**, *129*, 8139.
(60) Bagai, R.; Wernsdorfer, W.; Abboud, K. A.; Christou, G. *J. Am. Chem. Soc.* **2007**, *129*, 12918.

DOI: 10.1021/jacs.5b09378
J. Am. Chem. Soc. 2015, 137, 14406−14422

(61) Boskovic, C.; Bircher, R.; Tregenna-Piggott, P. L. W.; Güdel, H. U.; Paulsen, C.; Wernsdorfer, W.; Barra, A.-L.; Khatsko, E.; Neels, A.; Stoeckli-Evans, H. *J. Am. Chem. Soc.* **2003**, *125*, 14046.
(62) Wernsdorfer, W.; Aliaga-Alcalde, N.; Hendrickson, D. N.; Christou, G. *Nature* **2002**, *416*, 406.
(63) Das, A.; Gieb, K.; Krupskaya, Y.; Demeshko, S.; Dechert, S.; Klingeler, R.; Kataev, V.; Büchner, B.; Müller, P.; Meyer, F. *J. Am. Chem. Soc.* **2011**, *133*, 3433.
(64) Inglis, R.; Jones, L. F.; Mason, K.; Collins, A.; Moggach, S. A.; Parsons, S.; Perlepes, S. P.; Wernsdorfer, W.; Brechin, E. K. *Chem. - Eur. J.* **2008**, *14*, 9117.
(65) Inglis, R.; Taylor, S. M.; Jones, L. F.; Papaefstathiou, G. S.; Perlepes, S. P.; Datta, S.; Hill, S.; Wernsdorfer, W.; Brechin, E. K. *Dalton Trans.* **2009**, 9157.
(66) Nguyen, T. N.; Wernsdorfer, W.; Abboud, K. A.; Christou, G. *J. Am. Chem. Soc.* **2011**, *133*, 20688.
(67) Yang, E.-C.; Wernsdorfer, W.; Hill, S.; Edwards, R. S.; Nakano, M.; Maccagnano, S.; Zakharov, L. N.; Rheingold, A. L.; Christou, G.; Hendrickson, D. N. *Polyhedron* **2003**, *22*, 1727.
(68) Tiron, R.; Wernsdorfer, W.; Aliaga-Alcalde, N.; Christou, G. *Phys. Rev. B: Condens. Matter Mater. Phys.* **2003**, *68*, 140407.
(69) Guo, Y.-N.; Xu, G.-F.; Wernsdorfer, W.; Ungur, L.; Guo, Y.; Tang, J.; Zhang, H.-J.; Chibotaru, L. F.; Powell, A. K. *J. Am. Chem. Soc.* **2011**, *133*, 11948.
(70) Ramsey, C. M.; del Barco, E.; Hill, S.; Shah, S. J.; Beedle, C. C.; Hendrickson, D. N. *Nat. Phys.* **2008**, *4*, 277.
(71) Feng, X.; Mathonière, C.; Jeon, I.-R.; Rouzières, M.; Ozarowski, A.; Aubrey, M. L.; Gonzalez, M. I.; Clérac, R.; Long, J. R. *J. Am. Chem. Soc.* **2013**, *135*, 15880.
(72) Mathonière, C.; Lin, H.-J.; Siretanu, D.; Clérac, R.; Smith, J. M. *J. Am. Chem. Soc.* **2013**, *135*, 19083.
(73) Pinkowicz, D.; Ren, M.; Zheng, L.-M.; Sato, S.; Hasegawa, M.; Morimoto, M.; Irie, M.; Breedlove, B. K.; Cosquer, G.; Katoh, K.; Yamashita, M. *Chem. - Eur. J.* **2014**, *20*, 12502.
(74) Ren, M.; Pinkowicz, D.; Yoon, M.; Kim, K.; Zheng, L.-M.; Breedlove, B. K.; Yamashita, M. *Inorg. Chem.* **2013**, *52*, 8342.
(75) Norel, L.; Feng, M.; Bernot, K.; Roisnel, T.; Guizouarn, T.; Costuas, K.; Rigaut, S. *Inorg. Chem.* **2014**, *53*, 2361.
(76) Nava, A.; Rigamonti, L.; Zangrando, E.; Sessoli, R.; Wernsdorfer, W.; Cornia, A. *Angew. Chem., Int. Ed.* **2015**, *54*, 8777.
(77) Miyasaka, H.; Matsumoto, N.; Okawa, H.; Re, N.; Gallo, E.; Floriani, C. *J. Am. Chem. Soc.* **1996**, *118*, 981.
(78) Miyasaka, H.; Takahashi, H.; Madanbashi, T.; Sugiura, K.-i.; Clérac, R.; Nojiri, H. *Inorg. Chem.* **2005**, *44*, 5969.
(79) Tregenna-Piggott, P. L. W.; Sheptyakov, D.; Keller, L.; Klokishner, S. I.; Ostrovsky, S. M.; Palii, A. V.; Reu, O. S.; Bendix, J.; Brock-Nannestad, T.; Pedersen, K.; Weihe, H.; Mutka, H. *Inorg. Chem.* **2009**, *48*, 128.
(80) Dreiser, J.; Schnegg, A.; Holldack, K.; Pedersen, K. S.; Schau-Magnussen, M.; Nehrkorn, J.; Tregenna-Piggott, P.; Mutka, H.; Weihe, H.; Bendix, J.; Waldmann, O. *Chem. - Eur. J.* **2011**, *17*, 7492.
(81) Pedersen, K. S.; Schau-Magnussen, M.; Bendix, J.; Weihe, H.; Palii, A. V.; Klokishner, S. I.; Ostrovsky, S.; Reu, O. S.; Mutka, H.; Tregenna-Piggott, P. L. W. *Chem. - Eur. J.* **2010**, *16*, 13458.
(82) Dreiser, J.; Pedersen, K. S.; Schnegg, A.; Holldack, K.; Nehrkorn, J.; Sigrist, M.; Tregenna-Piggott, P.; Mutka, H.; Weihe, H.; Mironov, V. S.; Bendix, J.; Waldmann, O. *Chem. - Eur. J.* **2013**, *19*, 3693.
(83) McAuliffe, C. A.; Nabhan, A.; Pritchard, R. G.; Watkinson, M.; Bermejo, M.; Sousa, A. *Acta Crystallogr., Sect. C: Cryst. Struct. Commun.* **1994**, *50*, 1676.
(84) Ashmawy, F. M.; McAuliffe, C. A.; Parish, R. V.; Tames, J. *J. Chem. Soc., Dalton Trans.* **1985**, 1391.
(85) Hilfiger, M. G. Ph.D. Thesis, Texas A&M University, College Station, 2010.
(86) Howe, J. L. *J. Am. Chem. Soc.* **1896**, *18*, 981.
(87) Pedersen, K. S.; Dreiser, J.; Nehrkorn, J.; Gysler, M.; Schau-Magnussen, M.; Schnegg, A.; Holldack, K.; Bittl, R.; Piligkos, S.; Weihe, H.; Tregenna-Piggott, P.; Waldmann, O.; Bendix, J. *Chem. Commun.* **2011**, *47*, 6918.
(88) Cauzzi, D. A.; Mori, G.; Predieri, G.; Tiripicchio, A.; Cavatorta, F. *Inorg. Chim. Acta* **1993**, *204*, 181.
(89) Sheldrick, G. M. *Acta Crystallogr., Sect. A: Found. Crystallogr.* **2008**, *64*, 112.
(90) Barbour, L. J. *J. Supramol. Chem.* **2001**, *1*, 189.
(91) Chilton, N. F.; Anderson, R. P.; Turner, L. D.; Soncini, A.; Murray, K. S. *J. Comput. Chem.* **2013**, *34*, 1164.
(92) O'Connor, C. J. *Prog. Inorg. Chem.* **1982**, *29*, 203.
(93) Myers, B. E.; Berger, L.; Friedberg, S. A. *J. Appl. Phys.* **1969**, *40*, 1149.
(94) Richard, D.; Ferrand, M.; Kearley, G. J. *J. Neutron Res.* **1996**, *4*, 33.
(95) Lebedev, V. I.; Laikov, D. N. *Dokl. Math.* **1999**, *366*, 741.
(96) Stoll, S.; Schweiger, A. *J. Magn. Reson.* **2006**, *178*, 42.
(97) Lehn, J. M. *Supramolecular Chemistry: Concepts and Perspectives*; Wiley-VCH: Weinheim, 1995.
(98) Steed, J.; Atwood, J. L. *Supramolecular Chemistry*; John Wiley & Sons Ltd: Chichester, 2000.
(99) Costa, J. S. n.; Bandeira, N. A. G.; Le Guennic, B.; Robert, V.; Gamez, P.; Chastanet, G.; Ortiz-Frade, L.; Gasque, L. *Inorg. Chem.* **2011**, *50*, 5696.
(100) Schnegg, A.; Behrends, J.; Lips, K.; Bittl, R.; Holldack, K. *Phys. Chem. Chem. Phys.* **2009**, *11*, 6820.
(101) Dreiser, J.; Waldmann, O.; Dobe, C.; Carver, G.; Ochsenbein, S. T.; Sieber, A.; Güdel, H. U.; van Duijn, J.; Taylor, J.; Podlesnyak, A. *Phys. Rev. B: Condens. Matter Mater. Phys.* **2010**, *81*, 024408.
(102) Ferbinteanu, M.; Miyasaka, H.; Wernsdorfer, W.; Nakata, K.; Sugiura, K.-i.; Yamashita, M.; Coulon, C.; Clérac, R. *J. Am. Chem. Soc.* **2005**, *127*, 3090.
(103) Aubin, S. M. J.; Sun, Z.; Pardi, L.; Krzystek, J.; Folting, K.; Brunel, L.-C.; Rheingold, A. L.; Christou, G.; Hendrickson, D. N. *Inorg. Chem.* **1999**, *38*, 5329.
(104) Lecren, L.; Wernsdorfer, W.; Li, Y.-G.; Vindigni, A.; Miyasaka, H.; Clérac, R. *J. Am. Chem. Soc.* **2007**, *129*, 5045.

DOI: 10.1021/jacs.5b09378
J. Am. Chem. Soc. 2015, 137, 14406−14422